Numerical Simulations of the Nonlinear Quantum Vacuum in the Heisenberg-Euler Weak-Field Expansion

Andreas Lindner[a], Baris Ölmez[a], Hartmut Ruhl[a]

[a]*Ludwig-Maximilians-Universität München*
Theresienstr.37, 80333 München, Germany

Abstract

A numerical scheme for solving the nonlinear Heisenberg-Euler equations in up to three spatial dimensions plus time is presented and its properties are discussed. The algorithm is tested in one spatial dimension against a set of already known analytical results of vacuum effects such as birefringence and harmonic generation. Its power to go beyond analytically solvable scenarios is demonstrated in 2D. First parallelization scaling tests are conducted in 3D.

Keywords: Vacuum Polarization, Heisenberg-Euler, Weak-Field Expansion, Simulation, High Harmonics, Birefringence
2021 MSC:

1. Introduction

Virtual electron-positron pairs in the QED vacuum can mediate effective photon-photon interactions. Taking those into account in the low-energy limit below the Compton scale of the electron, nonlinear terms in the electromagnetic field extend Maxwell's theory. Radiation on the other hand can influence the behavior of the particle-antiparticle dipoles in the vacuum. Therefore, the vacuum of QED with its quantum fluctuations acts as a nonlinear, polarizable medium with quantifiable effects.

The corresponding low-energy effective theory was devised by Heisenberg and Euler [1]. Schwinger incorporated the theory into the larger QED picture [2].

There are numerous non-intuitive effects beside the commonly known Casimir effect and Lamb shift that are due to the quantum nature of the vacuum. Among those are vacuum birefringence [3–5], polarization rotation [6], vacuum diffraction [7–10], dispersion [11], scattering [12], reflection [13], generation of higher harmonics [14, 15], or photon merging [14, 16, 17] and photon splitting [11, 18, 19].

A promising approach to their detection is the investigation of the asymptotic dynamics of *probe* photons after the collision with high-intensity laser pulses. Due to their nonlinear interaction with the power pulses, probe photons scatter in such a way that their dynamics or polarization distinguishes them from the latter. The properties and dynamics of the quantum vacuum, in turn, are hereby encoded into the probe photons.

Nowadays the measurement of nonlinear vacuum effects is either possible or within reach thanks to the tremendous progress in high-intensity laser technology in recent years [20, 21].

Almost all analytical approaches found in the literature to compute nonlinear vacuum effects, e.g. as in [7, 12, 14, 17, 22–35] have shortcomings. As a consequence these attempts are still limited to simple scenarios which most of the time are inappropriate for experimental verification.

The present paper introduces a numerical algorithm for the solution of the weak-field approximation of the Heisenberg-Euler equations [36, 37] [15]. In [36, 37] the numerical scheme outlined in 1D in [15] is extended to full 3D simulations while at the same time the computational load is reduced. The accuracy of the numerical algorithm in [36, 37] relies on the assumptions that the fields vary on scales larger than the Compton scale of the electron and the field strengths involved are below the *critical* field for pair creation in the vacuum. In addition, a viable numerical algorithm is restricted by the computational load it generates especially in the realm of high frequencies. The advantage, however, of a numerical approach is that it can principally solve any interaction scenario for any arrangement of laser pulses.

The numerical predictions of the algorithm are benchmarked with analytical predictions of birefringence as calculated in [25, 26] and higher harmonics as predicted in [17].

1.1. Outline

The paper begins with a recap of the weak-field expansion of the Heisenberg-Euler effective theory. In Maxwell's theory, where there are no light-light interactions, the superposition principle for the set of differential equations holds, i.e., they are linear. In section 3, the nonlinear modifications to Maxwell's equations due to the Heisenberg-Euler theory are shown. In section 4 the simulation algorithm that solves the nonlinear Maxwell equations in 3+1 dimensions is introduced. In sections 6-9 the power of the Heisenberg-Euler solver is demonstrated by solving various scenarios of nonlinear vacuum phenomena and by successfully benchmarking with analytical results where they exist. In section 6 the phase velocity reduction of a probe pulse propagating through a strong electromagnetic background is successfully compared to analytical predictions for sufficiently large background field strengths. In section 7 the phenomenon of vacuum birefringence is investigated with the help of simulations for probe-pump setups. The theoretical prediction of the the flipping probability is verified and an analytical value of the latter for a special setting computed in [25] is reproduced. In section 8 the capability of the simulation algorithm to predict higher harmonics in the vacuum is demonstrated. It is shown that for specific settings analytical results from [17] are accurately reproduced in the simulations presented in this work. Examples of 2D simulations are presented in section 9. The latter are hard, if not impossible, to obtain by analytical means. The 2D results are used for comparison with the previous 1D simulations. Higher-dimensional simulations enable the investigation of complicated scenarios that cannot be solved analytically in the future. The paper is concluded with a summary and an outlook to future research employing the Heisenberg-Euler solver in section 10.

2. Heisenberg-Euler Lagrangian

Following the derivation by Schwinger [2] the Heisenberg-Euler Lagrangian reads

$$\mathcal{L}_{HE} = -\frac{c^5 m^4}{8\hbar^3 \pi^2} \int_0^\infty \frac{e^{-s}}{s^3} \left(\frac{s^2}{3} \left(a^2 - b^2 \right) - 1 + abs^2 \cot(as) \coth(bs) \right) ds \; , \tag{1}$$

where

$$a = \sqrt{\sqrt{\mathcal{F}^2 + \mathcal{G}^2} + \mathcal{F}} \; , \quad b = \sqrt{\sqrt{\mathcal{F}^2 + \mathcal{G}^2} - \mathcal{F}} \; , \tag{2}$$

$$\mathcal{F} = -\frac{c^2 F^{\mu\nu} F_{\mu\nu}}{4 E_{cr}^2} \; , \quad \mathcal{G} = -\frac{c^2 F^{\mu\nu} F_{\mu\nu}^*}{4 E_{cr}^2} \; , \tag{3}$$

$$E_{cr} = \frac{m^2 c^3}{e\hbar} = 1.3 \times 10^{18} \frac{\text{V}}{\text{m}} \; . \tag{4}$$

The quantities F and F^* denote the electromagnetic tensor and its dual and E_{cr} is the critical field strength, which is an important scale for the magnitude of the vacuum nonlinearities. The Lagrangian for the quantum vacuum is given by

$$\mathcal{L} = \frac{c^5 m^4}{\hbar^3} \mathcal{L}_{MW} + \mathcal{L}_{HE} = \frac{c^5 m^4}{\hbar^3} \mathcal{F} + \mathcal{L}_{HE} \quad \text{and} \quad \mathcal{L}_{MW} = \frac{c^5 m^4}{\hbar^3} \mathcal{F} \; , \tag{5}$$

where $\mathcal{L}_{MW}$ is the normalized free Maxwell Lagrangian. To derive $\mathcal{L}_{HE}$ it has been assumed that the constant background approximation is valid [38, 39] due to the fact that the variations of the field strengths are small on the scale of the Compton wavelength

$$\lambda_C = \frac{\hbar}{mc} = 2.426 \times 10^{-12} \text{m} \; . \tag{6}$$

Since the integral in (1) is hard to evaluate explicitly the so-called weak-field expansion is performed to simplify the integral expressions. The explicit form of the Heisenberg-Euler Lagrangian in the weak-field expansion up to the forth order in a and b is given by

$$\mathcal{L}_{HE} \approx \frac{c^5 m^4}{360\hbar^3 \pi^2} \left(4\mathcal{F}^2 + 7\mathcal{G}^2 \right) \tag{7a}$$

$$+ \frac{c^5 m^4}{630\hbar^3 \pi^2} \left(8\mathcal{F}^3 + 13\mathcal{F}\mathcal{G}^2 \right) \tag{7b}$$

$$+ \frac{c^5 m^4}{945\hbar^3 \pi^2} \left(48\mathcal{F}^4 + 88\mathcal{F}^2\mathcal{G}^2 + 19\mathcal{G}^4 \right) \; . \tag{7c}$$
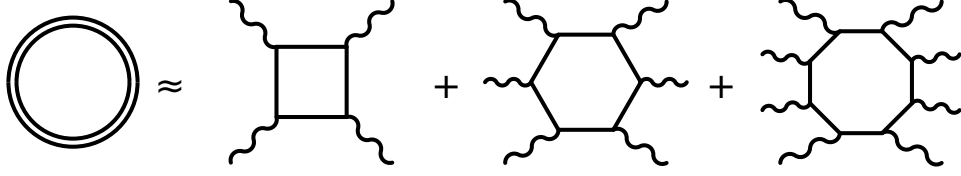
Figure 1: Depiction of the weak-field expansion of the Heisenberg-Euler Lagrangian. The double-lined loop to the left represents $\mathcal{L}_{HE}$ while the diagrams to the right are the 4-, 6-, and 8-photon contributions due to the weak-field expansion of $\mathcal{L}_{HE}$ corresponding to (7a),(7b), and (7c).

It should be noted that the Heisenberg-Euler Lagrangian solely depends on electromagnetic invariants and subsequently (7a) is of the order $\mathcal{O}((E/E_{cr})^4)$. The effective interaction $\mathcal{L}_{HE}$ can be graphically represented by a double-lined loop as in figure 1 to the left. As a consequence, (7a) represents the four-photon contributions, (7b) the six-photon contributions, and (7c) the eight-photon contribution to the closed loop as illustrated in figure 1. Since the electric field strength is normalized to the critical field strength with $c|F_{\mu\nu}| \ll E_{cr}$ higher order terms can be neglected in the low intensity regime.

It has to be mentioned that pair production is exponentially suppressed in the complete Heisenberg-Euler Lagrangian for $c|F_{\mu\nu}| \ll E_{cr}$. Therefore, the properties of the nonlinear vacuum can be described exclusively by radiation fields.

3. Modified Maxwell Equations

To obtain the nonlinear modifications to the linear Maxwell equations an explicit rescaling of the Maxwell Lagrangian to the critical field strengths is performed

$$\mathcal{L}_{MW} = -\frac{1}{4\mu_0} F^{\mu\nu} F_{\mu\nu} \xrightarrow{E \to \frac{E}{E_{cr}}} \mathcal{L}_{MW} = -\frac{1}{4\mu} F^{\mu\nu} F_{\mu\nu} \tag{8}$$

with the vacuum permeability

$$\mu_0 = 1.257 \times 10^{-6} \frac{\text{kg m}}{\text{s}^2 \text{A}^2} \tag{9}$$

and the definition

$$\mu = \frac{\hbar^2 e^2}{m^4 c^6} \mu_0 = 7.176 \times 10^{-43} \frac{\text{s}^4}{\text{kg m}} \ . \tag{10}$$

From the Lagrangian of the quantum vacuum (5) the equations of motion are obtained with the help of the Euler-Lagrange equations

$$\partial_t \left(\vec{E} + \mu \frac{\partial \mathcal{L}_{HE}}{\partial \vec{E}} \right) = \nabla \times \left(\vec{B} - \mu \frac{\partial \mathcal{L}_{HE}}{\partial \vec{B}} \right) \ . \tag{11}$$

The classical Maxwell equations [40]

$$\partial_t \vec{B} = -\nabla \times \vec{E} \ , \tag{12a}$$

$$\partial_t \left(\vec{E} + \vec{P} \right) = \nabla \times \left(\vec{B} - \vec{M} \right) \tag{12b}$$

are compared to (11) in such a way that photon-photon interactions are included, which implies the appearance of macroscopic nonlinear polarization and magnetization terms given by

$$\vec{P} = \mu \frac{\partial \mathcal{L}_{HE}}{\partial \vec{E}} \quad \text{and} \quad \vec{M} = \mu \frac{\partial \mathcal{L}_{HE}}{\partial \vec{B}}. \tag{13}$$

4. Numerical Method and Dispersion Effects

Recalling the two modified Maxwell equations (12) these equations are merged and a single partial differential equation that describes the whole dynamics of the system is formulated. The curl of $(\vec{B} - \vec{M})$

can be written as

$$\nabla \times (\vec{B} - \vec{M}) = \underbrace{\begin{pmatrix} 0 & 0 & 0 \\ 0 & 0 & -1 \\ 0 & 1 & 0 \end{pmatrix}}_{\mathbf{Q}_x} \partial_x (\vec{B} - \vec{M}) + \underbrace{\begin{pmatrix} 0 & 0 & 1 \\ 0 & 0 & 0 \\ -1 & 0 & 0 \end{pmatrix}}_{\mathbf{Q}_y} \partial_y (\vec{B} - \vec{M})$$

$$+ \underbrace{\begin{pmatrix} 0 & -1 & 0 \\ 1 & 0 & 0 \\ 0 & 0 & 0 \end{pmatrix}}_{\mathbf{Q}_z} \partial_z (\vec{B} - \vec{M}) = \sum_{j \in \{x;y;z\}} \mathbf{Q}_j \partial_j (\vec{B} - \vec{M}) , \tag{14}$$

with the help of (13), (14), and the vector

$$\vec{f} = \left(\vec{E}, \vec{B} \right)^{\mathrm{T}} , \tag{15}$$

where $\vec{E}$ and $\vec{B}$ are the electric and magnetic fields, (12) results in

$$(\mathbf{1}_6 + \mathbf{A}) \, \partial_t \vec{f} = \sum_{j \in \{x;y;z\}} \mathbf{Z}_j \partial_j \vec{f}. \tag{16}$$

The matrices $\mathbf{A}$ and $\mathbf{Z}_j$ are given by

$$\mathbf{A} = \begin{pmatrix} \mathbf{J}_{\vec{P}}\left(\vec{E}\right) & \mathbf{J}_{\vec{P}}\left(\vec{B}\right) \\ \mathbf{0}_3 & \mathbf{0}_3 \end{pmatrix} , \quad \mathbf{Z}_j = \begin{pmatrix} -\mathbf{Q}_j \mathbf{J}_{\vec{M}}\left(\vec{E}\right) & \mathbf{Q}_j - \mathbf{Q}_j \mathbf{J}_{\vec{M}}\left(\vec{B}\right) \\ -\mathbf{Q}_j & \mathbf{0}_3 \end{pmatrix} , \tag{17}$$

where

$$\mathbf{J}_{\vec{P}}(\vec{E}) = \frac{\partial \vec{P}}{\partial \vec{E}} , \quad \mathbf{J}_{\vec{P}}(\vec{B}) = \frac{\partial \vec{P}}{\partial \vec{B}} , \quad \mathbf{J}_{\vec{M}}(\vec{E}) = \frac{\partial \vec{M}}{\partial \vec{E}} , \quad \mathbf{J}_{\vec{M}}(\vec{B}) = \frac{\partial \vec{M}}{\partial \vec{B}} . \tag{18}$$

Equations (16) contain the full dynamics of the electromagnetic fields in weak-field approximation of the Heisenberg-Euler model. For simplicity, first the linear vacuum is considered by setting $\vec{P} = \vec{M} = 0$ leading to

$$\partial_t \vec{f} = \sum_{j \in \{x;y;z\}} \mathbf{Z}_j^{\mathrm{lin}} \partial_j \vec{f} , \quad \mathbf{Z}_j^{\mathrm{lin}} = \begin{pmatrix} 0 & \mathbf{Q}_j \\ -\mathbf{Q}_j & 0 \end{pmatrix} . \tag{19}$$

For later purposes $\mathbf{Z}_j^{\mathrm{lin}}$ is diagonalized using the rotation matrices

$$\mathbf{R}_x = \frac{1}{\sqrt{2}} \begin{pmatrix} \sqrt{2} & 0 & 0 & 0 & 0 & 0 \\ 0 & 1 & 0 & 0 & 0 & -1 \\ 0 & 0 & 1 & 0 & 1 & 0 \\ 0 & 0 & 0 & \sqrt{2} & 0 & 0 \\ 0 & 1 & 0 & 0 & 0 & 1 \\ 0 & 0 & 1 & 0 & -1 & 0 \end{pmatrix} , \quad \mathbf{R}_y = \frac{1}{\sqrt{2}} \begin{pmatrix} 0 & \sqrt{2} & 0 & 0 & 0 & 0 \\ -1 & 0 & 0 & 0 & 0 & -1 \\ 0 & 0 & -1 & 1 & 0 & 0 \\ 0 & 0 & 0 & 0 & \sqrt{2} & 0 \\ -1 & 0 & 0 & 0 & 0 & 1 \\ 0 & 0 & -1 & -1 & 0 & 0 \end{pmatrix} ,$$

$$\mathbf{R}_z = \frac{1}{\sqrt{2}} \begin{pmatrix} 0 & 0 & \sqrt{2} & 0 & 0 & 0 \\ 1 & 0 & 0 & 0 & -1 & 0 \\ 0 & 1 & 0 & 1 & 0 & 0 \\ 0 & 0 & 0 & 0 & 0 & \sqrt{2} \\ 1 & 0 & 0 & 0 & 1 & 0 \\ 0 & 1 & 0 & -1 & 0 & 0 \end{pmatrix} , \tag{20}$$

so that for $\mathbf{Z}_j^{\mathrm{lin}}$ the expressions

$$\mathbf{Z}_j^{\mathrm{lin}} = \mathbf{R}_j^{\mathrm{T}} \begin{pmatrix} 0 & 0 & 0 & 0 & 0 & 0 \\ 0 & 1 & 0 & 0 & 0 & 0 \\ 0 & 0 & 1 & 0 & 0 & 0 \\ 0 & 0 & 0 & 0 & 0 & 0 \\ 0 & 0 & 0 & 0 & -1 & 0 \\ 0 & 0 & 0 & 0 & 0 & -1 \end{pmatrix} \mathbf{R}_j = \mathbf{R}_j^{\mathrm{T}} \mathrm{diag}(0, 1, 1, 0, -1, -1) \mathbf{R}_j \tag{21}$$

are obtained. Now (19) becomes

$$\partial_t \mathbf{R}_j \vec{f}(x,y,z) = \text{diag}(0,1,1,0,-1,-1)\, \partial_j \mathbf{R}_j \vec{f}(x,y,z)\ , \tag{22}$$

where

$$\mathbf{R}_x \vec{f} = \frac{1}{\sqrt{2}} \begin{pmatrix} \sqrt{2}E_x \\ E_y - B_z \\ E_x + B_y \\ \sqrt{2}B_x \\ E_y + B_z \\ E_z - B_y \end{pmatrix} \quad , \quad \mathbf{R}_y \vec{f} = \frac{1}{\sqrt{2}} \begin{pmatrix} \sqrt{2}E_y \\ -B_z - E_x \\ B_x - E_z \\ \sqrt{2}B_y \\ B_z - E_x \\ -B_x - E_z \end{pmatrix} \quad , \quad \mathbf{R}_z \vec{f} = \frac{1}{\sqrt{2}} \begin{pmatrix} \sqrt{2}E_z \\ -B_y + E_x \\ B_x + E_y \\ \sqrt{2}B_z \\ B_y + E_x \\ -B_x + E_y \end{pmatrix} . \tag{23}$$

Equations (22) and (23) imply backward propagation in x-direction of the field components $(E_y - B_z)$ and $(E_x + B_y)$, forward propagation of the field components $(E_y + B_z)$ and $(E_z - B_y)$, and non-propagation of the first and forth component. Analogously for the other directions.

For demonstration purposes only the x-direction is considered in the following. Next, the spatial derivative ∂_x is replaced by finite differences

$$\partial_t \left(\mathbf{R}_x \vec{f} \right)(x,y,z) = \mathcal{D}_x \left(\mathbf{R}_x \vec{f} \right)(x,y,z)\ , \tag{24}$$

where

$$\mathcal{D}_x \left(\mathbf{R}_x \vec{f} \right)(x,y,z) = \sum_\nu \frac{1}{\Delta_x} S_\nu \left(\mathbf{R}_x \vec{f} \right)(x + \nu \Delta_x, y, z)\ . \tag{25}$$

The S_ν are stencil matrices and Δ_x is the spatial resolution. Now the stencil matrices S_ν are derived with the help of a Taylor expansion of the function $g(x + \nu \Delta_x)$ around $\nu \Delta_x = 0$. The Taylor expansion of g to 6th order accuracy is given by

$$g(x + \nu \Delta_x) = g(x) + (k \cdot \Delta_x)\, g(x) + \frac{1}{2}(\nu \cdot \Delta_x)^2\, g''(x) + \frac{1}{6}(\nu \cdot \Delta_x)^3\, g'''(x) + \frac{1}{24}(\nu \cdot \Delta_x)^4\, g^{(4)}(x)$$
$$+ \frac{1}{120}(\nu \cdot \Delta_x)^5\, g^{(5)}(x) + \frac{1}{720}(\nu \cdot \Delta_x)^6\, g^{(6)}(x) + \mathcal{O}\left((\nu \cdot \Delta_x)^7 \right) . \tag{26}$$

For the finite difference approximation of the first derivative the forward and backward finite differences are used. For the values $\nu \in \{-3, ..., 3\}$ the expansion in matrix form reads

$$\begin{pmatrix} g(x - 3\Delta_x) \\ g(x - 2\Delta_x) \\ g(x - \Delta_x) \\ g(x) \\ g(x + \Delta_x) \\ g(x + 2\Delta_x) \\ g(x + 3\Delta_x) \end{pmatrix} = \begin{pmatrix} 1 & -3 & 9/2 & -9/2 & 27/8 & -81/40 & 81/80 \\ 1 & -2 & 2 & -4/3 & 2/3 & -4/15 & 4/45 \\ 1 & -1 & 1/2 & -1/6 & 1/24 & -1/120 & 1/720 \\ 1 & 0 & 0 & 0 & 0 & 0 & 0 \\ 1 & 1 & 1/2 & 1/6 & 1/24 & 1/120 & 1/720 \\ 1 & 2 & 2 & 4/3 & 2/3 & 4/15 & 4/45 \\ 1 & 3 & 9/2 & 9/2 & 27/8 & 81/40 & 81/80 \end{pmatrix} \cdot \begin{pmatrix} g(x) \\ \Delta_x g'(x) \\ \Delta_x^2 g''(x) \\ \Delta_x^3 g'''(x) \\ \Delta_x^4 g^{(4)}(x) \\ \Delta_x^5 g^{(5)}(x) \\ \Delta_x^6 g^{(6)} x) \end{pmatrix} . \tag{27}$$

To illustrate how the finite difference approximation of the first derivative is calculated $\nu \in \{0, 1\}$ is considered, for simplicity. It is obtained

$$\begin{pmatrix} g(x) \\ g(x + \Delta_x) \end{pmatrix} = \begin{pmatrix} 1 & 0 \\ 1 & 1 \end{pmatrix} \cdot \begin{pmatrix} g(x) \\ \Delta_x g'(x) \end{pmatrix} , \tag{28}$$

which leads to the first derivative of g given by

$$g'(x) \approx g'_{\nu \in \{0,1\}} = \frac{g(x + \Delta_x) - g(x)}{\Delta_x}\ . \tag{29}$$

5

The derivative $g'_{\nu\in\{0,1\}}$ in (29) is called first order forward discrete derivative. In the same way the first order backward discrete derivative $g'_{\nu\in\{-1,0\}}$ is obtained with the help of

$$\begin{pmatrix} g(x - \Delta_x) \\ g(x) \end{pmatrix} = \begin{pmatrix} 1 & -1 \\ 1 & 0 \end{pmatrix} \cdot \begin{pmatrix} g(x) \\ \Delta_x g'(x) \end{pmatrix}, \tag{30}$$

where

$$g'_{\nu\in\{-1,0\}} = \frac{g(x) - g(x - \Delta_x)}{\Delta_x}. \tag{31}$$

In order to obtain specific dispersion properties and numerical stability of the discretized equations (22) it is necessary to introduce forward and backward finite differences for $\mathcal{D}_x$ as will be discussed below. Recall from (25) that

$$\partial_x \vec{f}(x, y, z) = \mathbf{R}_x^{\mathrm{T}} \partial_x \mathbf{R}_x \vec{f}(x, y, z) \approx \mathbf{R}_x^{\mathrm{T}} \sum_\nu \frac{1}{\Delta_x} S_\nu \left(\mathbf{R}_x \vec{f} \right)(x + \nu\Delta_x, y, z) = \mathbf{R}_x^{\mathrm{T}} \mathcal{D}_x \left(\mathbf{R}_x \vec{f} \right)(x, y, z). \tag{32}$$

The first three elements of the field vector $\mathbf{R}_x \vec{f}$ represent forward propagating electromagnetic modes, while the last three components of the latter represent backward propagating ones as discussed above.

To investigate dispersion effects in the finite difference approximation an easy example is shown in the following. For the values $\nu \in \{-1, 0, 1\}$ the expansion in matrix form is given by

$$\begin{pmatrix} g(x - \Delta_x) \\ g(x) \\ g(x + \Delta_x) \end{pmatrix} = \begin{pmatrix} 1 & -1 & 1/2 \\ 1 & 0 & 0 \\ 1 & 1 & 1/2 \end{pmatrix} \cdot \begin{pmatrix} g(x) \\ \Delta_x g'(x) \\ \Delta_x^2 g''(x) \end{pmatrix}. \tag{33}$$

It has to be noted that equation (33) does not restrict ourselves to one specific kind of finite difference method. To obtain an expression for the first derivative the matrix in (33) has to be inverted. This leads to

$$\begin{pmatrix} g(x) \\ \Delta_x g'(x) \\ \Delta_x^2 g''(x) \end{pmatrix} = \begin{pmatrix} 0 & 1 & 0 \\ -1/2 & 0 & 1/2 \\ 1 & -2 & 1 \end{pmatrix} \cdot \begin{pmatrix} g(x - \Delta_x) \\ g(x) \\ g(x + \Delta_x) \end{pmatrix}. \tag{34}$$

Let us assume that $g(x)$ is one of the two polarizations of an electromagnetic mode that propagates in positive $(+)$ or negative $(-)$ x-direction in 1D. Then the corresponding equation of motion reads

$$(\partial_t \pm c\, \partial_x)\, g_\pm(x; t) = 0. \tag{35}$$

Making use of (34) equation (35) becomes for symmetric forward and backward differentiation

$$\partial_t g_\pm(x; t) \pm \frac{c}{2\Delta_x} \left(g_\pm(x + \Delta_x; t) - g_\pm(x - \Delta_x; t) \right) = 0, \tag{36}$$

where the spatial derivative of g is accurate up to second order in Δ_x. Equation (36) can be solved analytically by a plane wave ansatz

$$g_\pm(x; t) = e^{-i\omega t + ik_\pm x}, \tag{37}$$

where $k_+ > 0$ and $k_- < 0$ to obtain

$$-(\omega_R + i\omega_I) \pm \frac{c}{\Delta_x} \sin(k_\pm \Delta_x) = 0, \tag{38}$$

$$\omega = \pm \frac{c}{\Delta_x} \sin(k_\pm \Delta_x). \tag{39}$$

However, the derivative in (35) can also be approximated for a forward propagating mode g_+ by a first order forward finite difference. In this case (36) can be written as

$$\partial_t g_+(x;t) + \frac{c}{\Delta_x}\left(g_+(x+\Delta_x;t) - g_+(x;t)\right) = 0\,, \tag{40}$$

where the solution of (40) with $\omega \in \mathbb{C}$ reads

$$-\omega + \frac{c}{\Delta_x}\left(\sin(k_+\Delta_x) + i - i\cos(k_+\Delta_x)\right) = 0\,, \tag{41}$$

$$\mathfrak{Re}(\omega) = \frac{c}{\Delta_x}\sin(k_+\Delta_x)\,, \tag{42}$$

$$\mathfrak{Im}(\omega) = \frac{c}{\Delta_x}\left(1 - \cos(k_+\Delta_x)\right)\,. \tag{43}$$

Next, the derivative in (35) for the backward propagating part can be approximated by a first order backward finite difference. In this case (36) can be approximated for the backward propagating case as

$$\partial_t g_-(x;t) - \frac{c}{\Delta_x}\left(g_-(x;t) - g_-(x-\Delta_x;t)\right) = 0 \tag{44}$$

with the solution

$$-\omega - \frac{c}{\Delta_x}\left(\sin(k_-\Delta_x) - i + i\cos(k_-\Delta_x)\right) = 0\,, \tag{45}$$

$$\mathfrak{Re}(\omega) = -\frac{c}{\Delta_x}\sin(k_-\Delta_x)\,, \tag{46}$$

$$\mathfrak{Im}(\omega) = \frac{c}{\Delta_x}\left(1 - \cos(k_-\Delta_x)\right)\,. \tag{47}$$

The dispersion relations connect a simulated wave with a specified wavelength to its phase velocity on the lattice. While in the symmetric case there is no imaginary part of ω, it does show up for antisymmetric differentiation. The derived dispersion relations are shown on the left and in the middle of figure 2 for the vacuum speed of light c set to 1. The Nyquist frequency $f_{Ny} = \Delta^{-1}/2$, corresponding to $k\cdot\Delta = \pi$, marks the point where $\mathfrak{Re}(\omega) = 0$ in all cases.
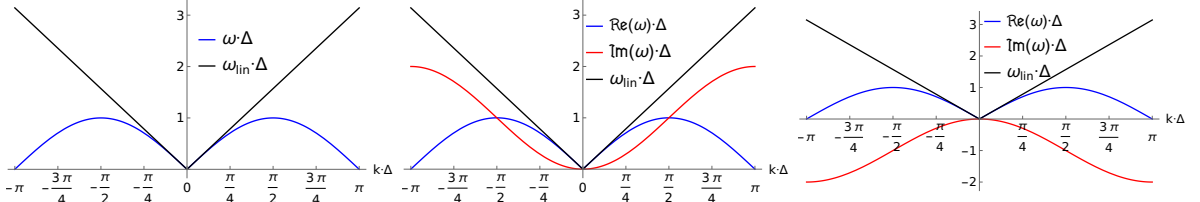

Figure 2: Dispersion relations obtained with low order finite differences for a simple plane wave. Left: for a second order symmetric forward and backward finite difference scheme. Middle: for a first order forward finite difference for the forward propagating part and a first order backward finite difference for the backward propagating part. Right: for a first order forward finite difference for the backward propagating part and a first order backward finite difference for the forward propagating part. The linear vacuum is given as the black line for reference.

The imaginary part amplifies the wave and thus makes this scheme unstable. By differentiating biased against the propagation direction however, the imaginary part switches signs and has a damping effect. The calculations are straightforward and the result is shown on the right of figure 2. This behavior can be tuned with higher order schemes in order to get a more vacuum-like real part and to defer the imaginary part such that it becomes relevant only for short wavelengths and damps them. As the real part of ω eventually decreases in any scheme, the damping of those waves will serve as anti-aliasing effect. This is shown below.

Furthermore, when the differentiation is chosen to be balanced, then $S_\nu = 0$, see e.g. (36). This implies that the derivative of g is independent of g itself which causes numerical instabilities in the form of mesh drifts [41]. Biasing the derivatives combats these instabilities but in turn causes a non-isotropic simulation space. The propagation speed of waves decreases in the direction, where the stencil is heavier weighted. The effects on the phase velocity by the non-isotropic space are also eased by applying the backward biased differentiation to the forward propagating components and vice versa.

Now, the unbalanced coefficients for the first order discrete derivative in fourth order accuracy in Δ_x, $g'_{\nu\in\{-3,1\}}$ and $g'_{\nu\in\{-1,3\}}$ in the above notation, are derived with the help of (27). This results in

$$\Delta_x g'_{\nu\in\{-3,1\}} = \begin{pmatrix} -1/12 & 1/2 & -3/2 & 5/6 & 1/4 \end{pmatrix} \begin{pmatrix} g(x-3\Delta_x) \\ g(x-2\Delta_x) \\ g(x-\Delta_x) \\ g(x) \\ g(x+\Delta_x) \end{pmatrix},$$

(48)

$$\Delta_x g'_{\nu\in\{-1,3\}} = \begin{pmatrix} -1/4 & -5/6 & 3/2 & -1/2 & 1/12 \end{pmatrix} \begin{pmatrix} g(x-\Delta_x) \\ g(x) \\ g(x+\Delta_x) \\ g(x+2\Delta_x) \\ g(x+3\Delta_x) \end{pmatrix}.$$

To make the connection to (24) g is replaced by the components of $\mathbf{R}_x\vec{f}$. As explained above, $\mathbf{R}_x\vec{f}$ has components propagating in different directions that are differentiated with biases in the respective opposite direction. This means that the first three components of $\mathbf{R}_x\vec{f}$ are differentiated as g in the first line of (48) and the last three components of $\mathbf{R}_x\vec{f}$ are differentiated as g in the second line of (48). Following these instructions for equation (25) yields

$$\mathcal{D}_x\left(\mathbf{R}_x\vec{f}\right)(x,y,z) = \sum_{\nu=-3}^{3} \frac{1}{\Delta_x} S_\nu \left(\mathbf{R}_x\vec{f}\right)(x+\nu\Delta_x,y,z) \tag{49}$$

with the stencils given by

$$S_{+3} = \frac{1}{\Delta_x}\mathrm{diag}(1/12,1/12,1/12,0,0,0), \qquad S_{-3} = \frac{1}{\Delta_x}\mathrm{diag}(0,0,0,-1/12,-1/12,-1/12),$$

$$S_{+2} = \frac{1}{\Delta_x}\mathrm{diag}(-1/2,-1/2,-1/2,0,0,0), \qquad S_{-2} = \frac{1}{\Delta_x}\mathrm{diag}(0,0,0,1/2,1/2,1/2),$$

$$S_{+1} = \frac{1}{\Delta_x}\mathrm{diag}(3/2,3/2,3/2,1/4,1/4,1/4), \qquad S_{-1} = \frac{1}{\Delta_x}\mathrm{diag}(-1/4,-1/4,-1/4,-3/2,-3/2,-3/2),$$

$$S_0 = \frac{1}{\Delta_x}\mathrm{diag}(-5/6,-5/6,-5/6,5/6,5/6,5/6).$$

(50)

The solver uses schemes of order thirteen. By going seven steps of Δ_x forward and six steps backward in the forward biased differentiation and vice versa in the backward biased case, the unbalance is kept small. The low-bias approximations to order thirteen are given by

$$\Delta_x g'_{\nu\in\{-7,6\}} = \big(-1/12012 \quad 1/792 \quad -1/110 \quad 1/24 \quad -5/36 \quad 3/8 \quad -1 \quad 1/7 \quad 3/4$$
$$-5/24 \quad 1/18 \quad -1/88 \quad 1/660 \quad -1/10296 \big) \cdot \begin{pmatrix} g(x-7\Delta_x) \\ \vdots \\ g(x+6\Delta_x) \end{pmatrix},$$

$$\Delta_x g'_{\nu\in\{-6,7\}} = \big(1/10296 \quad -1/660 \quad 1/88 \quad -1/18 \quad 5/24 \quad -3/4 \quad -1/7 \quad 1 \quad -3/8 \quad 5/36$$
$$-1/24 \quad 1/110 \quad -1/792 \quad 1/12012 \big) \cdot \begin{pmatrix} g(x-6\Delta_x) \\ \vdots \\ g(x+7\Delta_x) \end{pmatrix}.$$

(51)

For the nonlinear vacuum the system of ODEs is obtained from (16) to be

$$\partial_t \vec{f} = (\mathbf{1}_6 + \mathbf{A})^{-1} \sum_{j\in\{x,y,z\}} \mathbf{Z}_j \mathcal{D}_j \vec{f}. \tag{52}$$

The inversion of $(\mathbf{1}_6 + \mathbf{A})$ is an expensive operation. An approximation in terms of a truncated geometric series is not satisfying as also larger nonlinear corrections ought to be taken into account. The problem of inverting the matrix can be reduced from a 6×6 dimensional problem to a 3×3 dimensional one by making use of the block form in (17) such that [37]

$$(\mathbf{1}_6 + \mathbf{A})^{-1} = \begin{pmatrix} \mathbf{1}_3 + \mathbf{J}_{\vec{P}}\left(\vec{E}\right) & \mathbf{J}_{\vec{P}}\left(\vec{B}\right) \\ \mathbf{0}_3 & \mathbf{1}_3 \end{pmatrix} = \begin{pmatrix} \mathbf{C}^{-1} & -\mathbf{C}^{-1}\mathbf{J}_{\vec{P}}\left(\vec{B}\right) \\ \mathbf{0}_3 & \mathbf{1}_3 \end{pmatrix}, \tag{53}$$

with

$$\mathbf{C} = \mathbf{1}_3 + \mathbf{J}_{\vec{P}}\left(\vec{E}\right) . \tag{54}$$

This 3×3 matrix can be inverted explicitly.

For a single plane wave the Heisenberg-Euler Lagrangian reduces to the Maxwell Lagrangian as $\mathcal{F} = \mathcal{G} = 0$. The vacuum is the linear one. Inserting a forward propagating plane wave

$$\vec{E}(\vec{x};t) = \vec{A}\,e^{-i(\omega t - \vec{k}\cdot\vec{x})}$$

into the propagation equation (52) yields the constraint

$$\det\left(i\omega\mathbf{1}_6 + \sum_{j\in\{x,y,z\}} \mathbf{Z}^{\mathrm{lin}}\,\mathbf{R}_j^{\mathrm{T}} \sum_\nu S_\nu e^{i\nu k_j \Delta_j} \mathbf{R}_j\right) = 0 . \tag{55}$$

Solving for the real and imaginary parts of ω gives

$$\mathfrak{Re}(\omega) = \left\| \mathfrak{Im}\left(\sum_{j\in\{x,y,z\}} \sum_\nu S_\nu e^{i\nu k_j \Delta_j} \mathbf{Z}^{\mathrm{lin}}\right)\right\| \quad \text{and} \quad -\mathfrak{Im}(\omega) = \left\| \mathfrak{Re}\left(\sum_{j\in\{x,y,z\}} \sum_\nu S_\nu e^{i\nu k_j \Delta_j} \mathbf{Z}^{\mathrm{lin}}\right)\right\|, \tag{56}$$

where $\|\bullet\|$ denotes the matrix norm. The rotation matrices cancel in the final analytical expressions. The results are visualized in figure 3 for propagation along one axis with the stencils (50) and the stencils obtained from (51) which are the ones used for the simulations. The spacing between the lattice points Δ, the "resolution" of the lattice, is the decisive parameter to tune the dispersive effects for any given wavelength. It is given by the ratio of physical length and lattice points.
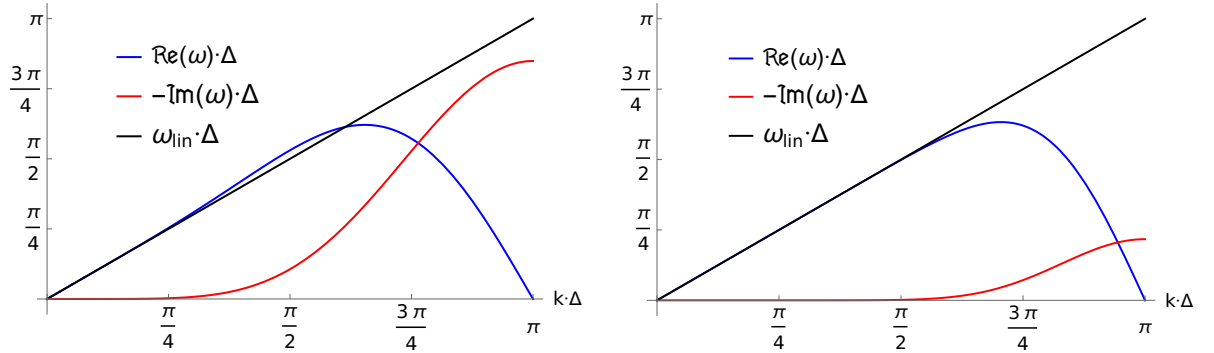

Figure 3: Plots of the real part of ω (blue), the imaginary part of ω (red) according to (55), and the linear vacuum (black), against k for asymmetric finite difference schemes of forth order (left) and thirteenth order (right). For better visibility of the symmetric plots only the values for $k \geq 0$ are shown. The trivial solution and negative frequency solutions of (55) are discarded.

It can be seen that for higher orders the real part stays close to the linear vacuum for smaller wavelengths. Higher orders also defer and decrease the rise of the imaginary part. A strong bias as in the forth order scheme (48) causes a superluminous phase-velocity in a given $k \cdot \Delta$ range. The well balanced order thirteen scheme is well behaved for a larger range of wavelengths. From figure 3, it can be deduced that the dispersion relation follows the continuous vacuum for up to $k \cdot \Delta \simeq \pi/2$. For smaller the wavelengths the curve showing the real part of ω falls off from the linear vacuum and the imaginary part of ω causes a damping. Due to the concavity of the real part there are two k's for each $\mathfrak{Re}(\omega)$. At the wavelength corresponding to the Nyquist frequency, $k \cdot \Delta = \pi$, $\mathfrak{Re}(\omega)$ becomes zero as in the cases above. The high-k values cause unphysical standing waves, as $\mathfrak{Re}(\omega)/k \to 0$, which would cause a self-heating of the system. The damping takes care of their annihilation à la "fire&forget". The superluminosity which can be seen in the forth order finite difference differentiation is thus an acceptable add-on to the favor of

a damping of unphysical modes. Increasing accuracy and balancing as in the 13 order scheme, there is no superluminous range left.

In the numerical investigation it is demonstrated that the damping has noticeable effects already at an earlier stage than a first look at the above plot would suggest. Note that the Nyquist frequency, on the other hand, $f_{Ny} = \Delta^{-1}/2$ (corresponding to $k \cdot \Delta = \pi$) is not the limiting factor for wave modelings in this numerical scheme. It has to be stayed well below the Nyquist limit for accurately time-evolved waves. Note that the simulation of a high frequency wave does not overshoot the Nyquist limit, as it would be sampled as a wave with lower frequency, see figure 4. The algorithm is stable for any frequency.
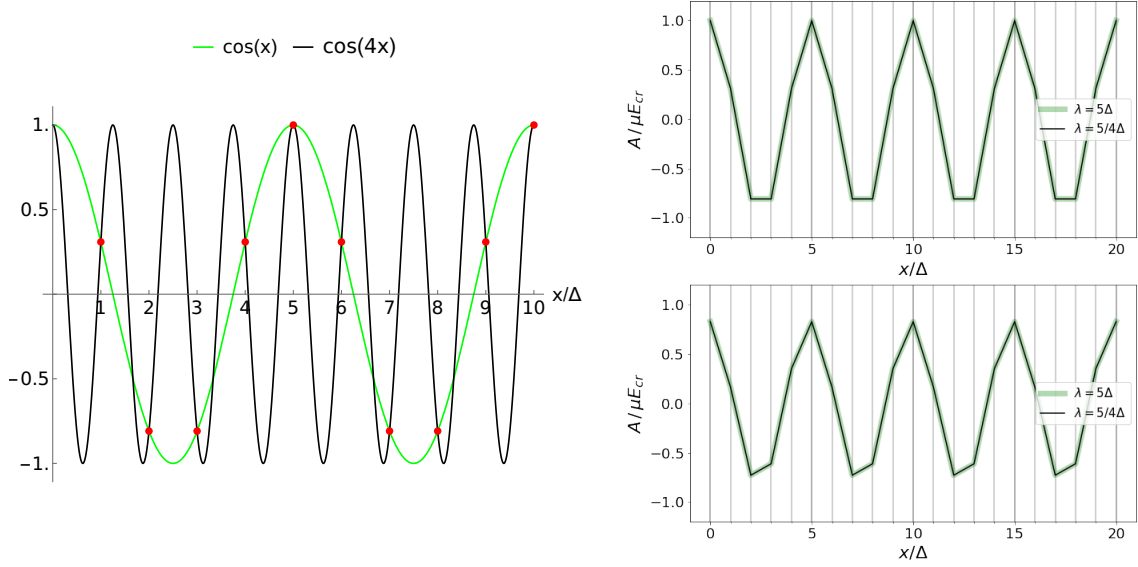
Figure 4: Effect of overshooting the Nyquist frequency. Left: Two cosine functions that when periodically evaluated at multiples of the distance $\Delta = 0.4\pi$ have the same values. Right: Simulations to verify the behavior on the grid. On a 1D line with point spacing $\Delta = 0.1\mu m$ two waves with wavelengths 5Δ and $5/4\Delta$ are simulated, corresponding to the analytical scenario on the left. It can be seen that the discretization makes no difference between the two. The simulated waves are shown in the initial state (top right) and after they have propagated the distance of 90 periods (bottom right). The damping effect due to the imaginary part of ω in the dispersion relation is the same for both waves.

To visualize the effects of the dispersion relation at varying wavelengths the propagation of a plane wave in a two dimensional square grid with side length $80\mu m$ divided into 1024×1024 points is investigated. The resolution is therefore given by $\Delta = 80\mu m/1024$, $\Delta^{-1} = 128 \times 10^5 m^{-1}$.
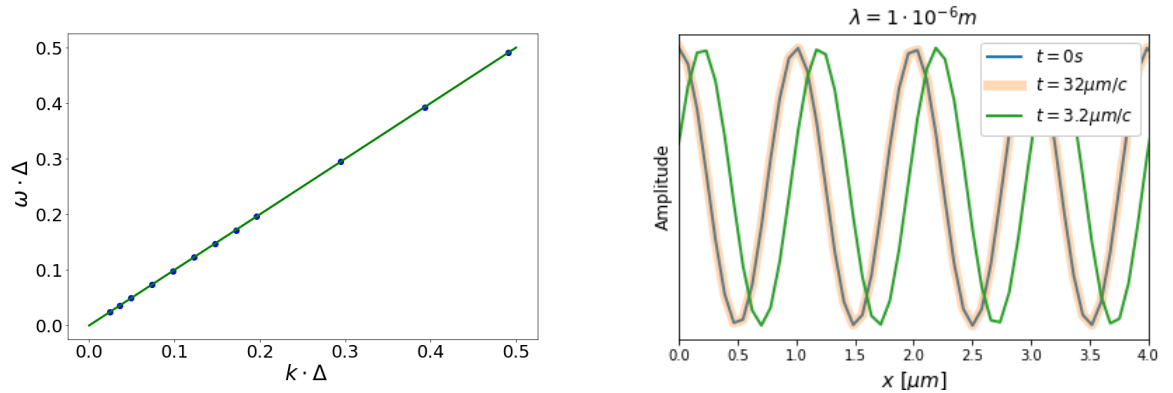

Figure 5: Left: The numerical results of the dispersion relation (blue dots) are in agreement with the free vacuum (green line) for wavelengths $20\mu m$ to $1\mu m$. The grid resolution is given by $\Delta = 80\mu m/1024$ in the propagation direction. Right: A plane wave with $\lambda = 1\mu m$ at different time steps. The wave does not lose energy – the amplitude stays the same. Even after 32 periods the waves are perfectly overlapping.

From figure 5 it can be deduced that the waves are well behaved and quite well modeled for $k \cdot \Delta \lesssim 0.5$.
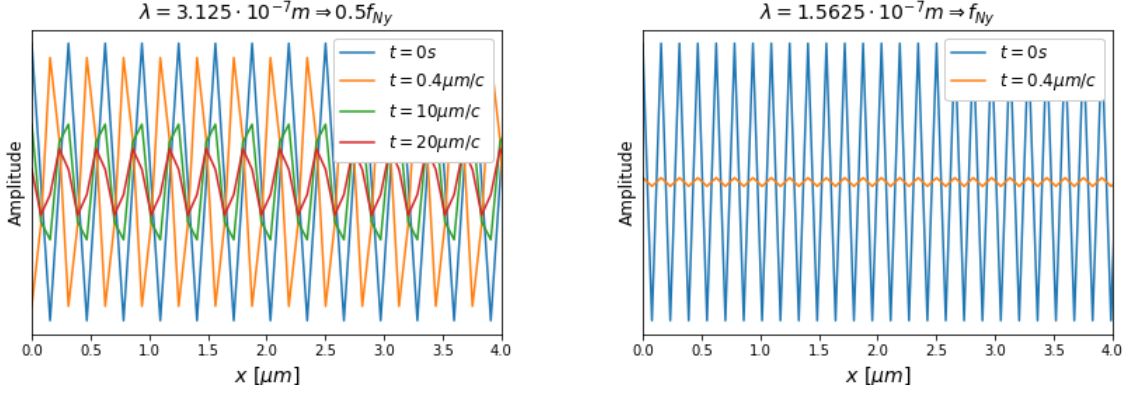
Figure 6: Left: A plane wave with $\lambda = 312.5nm$ at different time steps. The grid resolution is given by $\Delta = 80\mu m/1024$ in the propagation direction. In the free vacuum the corresponding frequency is to be associated to half the Nyquist frequency. 32 periods would have passed after $10\mu m/c$ and 62 periods after $20\mu m/c$. The damping and also the barely sub-luminous phase velocity are, after enough propagation time, noticeable even at this wavelength. The initial peak position has clearly shifted after $20\mu m/c$. Right: A plane wave with $\lambda = 156.25nm$ at different time steps with the same grid settings. In the free vacuum the corresponding frequency is to be associated to the Nyquist frequency. The wave is standing and the damping is strong. It annihilates the wave within less than a micro second.
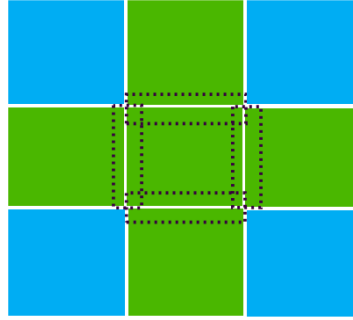

Figure 7: Ghost-cell exchange. The green cell in the middle exchanges its boundary values with those of the green neighboring cells. The boundary region is indicated by the black dashes. The blue cells at the corners do not interact with the cell in the middle. The analogous situation holds in 1D and 3D.

From figure 6, it can be inferred that already at half the Nyquist frequency the damping is non-negligible for relevant time scales. The Nyquist frequency in this scenario is given by $f_{Ny} = 64 \times 10^5 m^{-1}$ ($\lambda = 1.5625 \times 10^{-7}m$). The conclusion is that for a proper modeling and to avoid damping effects, one is obliged to adapt the grid resolutions to the lowest wavelength such that $\Delta \lesssim 1/12\,\lambda$. While this relation is not a hard limit and can be relaxed in many cases without detriments, it poses a safe rule of thumb. A sufficiently fine grid resolution is pertinent for a clean analysis of the polarization flipping and high harmonic generation effects in the present work.

5. Scaling Behavior

5.1. Solving the ODE and processing the data

For the numerical solution of the resulting system of ODEs for $\vec{f}$ (52) the Adams-Moulton ODE solver from CVODE is used, which is part of the SUNDIALS library [42]. The code writes the output data into a comma separated values (CSV) file for each user defined time step. The CSV file contains the six data columns for E_x, E_y, E_z, B_x, B_y, and B_z. Each of the six columns holds all the grid values for each of the field components. The post-processing of the data is done with the help of *Jupyter notebooks* employing the Python *SciPy* library and with the help of *Mathematica* [43–45].

5.2. Parallelization of the algorithm

For faster computation and scalability the code is parallelized. To this end the lattice is sliced allowing separate cores to process sub-lattices. The number of sub-lattices is given by splitting each dimension of the lattice into equal parts. The finite differences used to discretize derivatives require values from neighboring sub-lattices. Hence, ghost cells are placed at the boundaries of the latter, see figure 7. The ghost cells are updated via message passing making use of *MPI* [46]. The number of sub-lattices is equal to the size of the global communicator, i.e., the number of processes. Updating a given timestep n to $n+1$ by

computing the right hand side of (52) is a purely local operation. Since efficient parallelization is relevant for expensive 3D simulations a scaling test is conducted due to parallelization for the propagation of a single plane wave in a cube. To test the parallel speedup the runtimes of the code for wave propagation in x-direction with a wavelength of $4\mu m$ and amplitude $A = 1\mathrm{m}E_{cr} = 1\times10^{-3}E_{cr}$ polarized in y-direction is compared for varying core number. For the test no output data is generated. The total propagation time is 100fs divided into 100 steps. The used high-performance computing (HPC) system contains 16 cores per memory domain (here a socket) and two sockets per node. The results of the scaling test are visualized in figure 8. The code is at this scale clearly memory-bound as the behavior at the socket saturation shows.
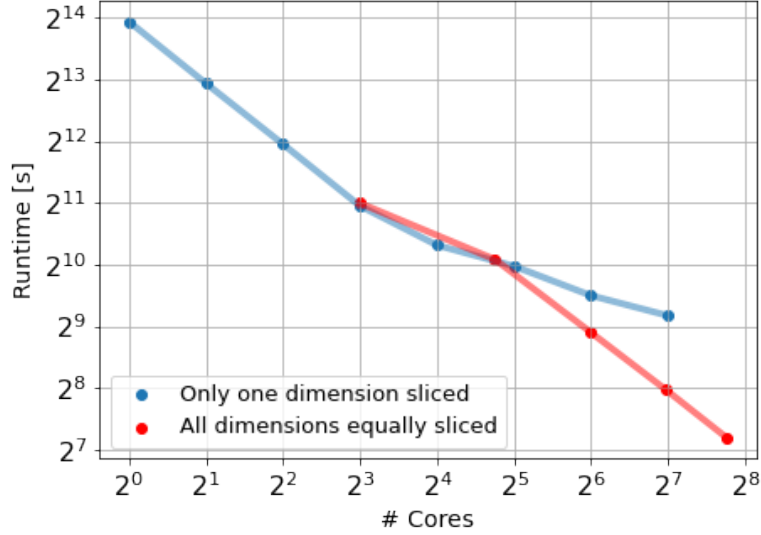
Lattice slicing only in one dimension

Number of Cores:	1	2	4	8	16	32	64	128
Average Runtime:	15692s	7838s	3960s	1979s	1273s	1006s	723s	577s

Equal slicing in every dimension

Number of Cores:	8	27	64	125	216
Average Runtime:	2041s	1083s	477s	252s	147s

Figure 8: Runtimes for the simulation of a plane wave of wavelength $4\mu m$ in a 3D cube with volume $80 \times 80 \times 80\,\mu m^3$ divided into $256 \times 256 \times 256$ points. Each setting is run twice and averaged in order to to take into account minor runtime variations. The runtimes nearly halve for a doubling of cores for up to 8 cores. The cube is here sliced into sub-lattices in the propagation direction of the wave (blue line and dots). The runtime speedup decreases where one memory domain (socket) is fully occupied with 16 cores. This is a typical feature for memory-bound code. The intra-socket scaling is not linear as the memory as a shared resource on the socket resource does not scale along with more used cores. The socket gets "saturated" due to memory bandwidth exhaustion when the memory interface struggles to keep up with the cores' access instructions. The cores demand more data to process than the memory interface is able to deliver. For inter-node scaling on the other hand the performance scales again along with cores and memory as parallel resources. Taking the number of nodes as baseline for the scaling test would thus be another choice. For inter-node scaling, it can be seen that slicing only in one dimension leads to a communication overhead when the sublattices become too narrow. This is remedied in this scenario by an equal slicing in every dimension (red line and dots). The scaling across nodes is then again linear.

Much larger scaling tests require exclusive computing time on a number of nodes of a high-performance computing system and are part of ongoing research. An example simulation of a plane wave in a box with 1000×1000×1000 on 256 cores, occupying full 8 nodes took about 20 hours on the same system used for the previous benchmarks. For larger 3D simulations like that the code becomes more and more MPI-bound. In the ongoing research the bottlenecks for larger simulations are investigated in detail with various HPC tools and the communication and computation scaling is improved by taking advantage of hardware affinity, vectorization, MPI virtual topologies, hybrid OpenMP+MPI parallelization, etc.

Next, the numerical complexity scaling of the algorithm and the employed solver with the grid size and dimension is calculated theoretically.

5.3. Computational complexity scaling of the algorithm

3D simulations run in a cube with $N = N_x \cdot N_y \cdot N_z$ equally spaced points $\mathcal{C} = \{x_{x,y,z} = (n_x \Delta_x, n_y \Delta_x, n_z \Delta_x) | n_i = 1, ..., N_i\} \subset \mathbb{R}^3$. The application of the algorithm is subdivided into three computations. The calculation of the derivatives of $\vec{f}$ as well as the right hand side of the ODE (52) followed by its integration.

In the first step the derivatives are approximated by finite differences. Therefore, the number of operations does not depend on the number of lattice points. Nevertheless, the derivatives have to be performed for each point and for each dimension explicitly. For the calculation of the derivatives the computational load $\mathbf{C}_D$ is obtained to be

$$\mathbf{C}_D \propto D \cdot N_x \cdot N_y \cdot N_z \,,$$

where D denotes the number of spatial dimensions.

Second, the computation on the right hand side of (52) has to be performed for each lattice point. The dimension-dependent summation causes an extra computational load by increasing D by 1. The computational load for the calculation of (52) $\mathbf{C}_M$ is given by

$$\mathbf{C}_M \propto N_x \cdot N_y \cdot N_z \cdot (D + 1) \,.$$

In the last step for the solution of (52) the computational load of the used ODE solver has to be taken into account. Hereby, the integration of the ODE highly depends on a wide range of considerations, such as involved frequencies or the magnitude of the nonlinearities. The computational load of the solver *CVODE* [42] $\mathbf{C}_S$ is

$$\mathbf{C}_S \propto N_x \cdot N_y \cdot N_z \cdot \Delta^{-1}.$$

Thus, for the upper limit of the problem with regards to the scaling behavior it is obtained

$$\mathbf{C} \propto N_x \cdot N_y \cdot N_z \cdot (D + 1) \cdot \Delta^{-1} \,.$$

Next, the backtesting of the algorithm in regimes where the dispersion relation is well-behaved is performed.

6. Phase Velocity in a Strong Background

A probe plane wave is propagated along the x-axis,

$$\vec{E}(x; t) = \vec{A} \cos(kx - kvt) \,, \tag{57}$$

through a linearly polarized strong electromagnetic background field. The polarization of the strong background breaks the isotropy of space, giving rise to different refractive indices [26, 47]

$$n_\pm = 1 + \frac{\alpha}{45\pi}(11 \pm 3)\frac{E^2}{E_{cr}^2} = 1 + \delta n_\pm \tag{58}$$

for a probe polarization orthogonal (+) and parallel (-) to the background polarization. Since (58) only takes into account the 4-photon interaction contribution, i.e., it neglects all but the first nonlinear term in (7), the results are verified turning off 6-photon processes in the simulations.

The phase shift caused by the nonlinear deviation from the vacuum speed of light is given by

$$v \to \frac{1}{1 + \delta n_\pm} \Rightarrow v_{\mathrm{nli}} = -\frac{\delta n_\pm}{1 + \delta n_\pm} \,. \tag{59}$$

Its contribution to the phase can be extracted by a Fourier analysis of the time-propagated wave. When the passed time of propagation is chosen to be an integer multiple of λ, it is obtained with $l \in \mathbb{N}$ [37]

$$\vec{E}(x; l \cdot t) = \vec{A} \cos(2\pi x/\lambda - 2\pi l \, v_{\mathrm{nli}}) = \vec{A} \cos(2\pi(x/\lambda - l \, v_{\mathrm{nli}})) \,. \tag{60}$$

The nonlinear phase value contribution can then be extracted from the phase after a spatial Fourier transformation evaluated at $1/\lambda$. This results in

$$v_{\mathrm{nli}} = -\frac{1}{2\pi l} \arg\left(\mathrm{FT}[E(x; t_l)](\lambda^{-1})\right) \quad \text{and} \quad t_l = l \cdot \lambda. \tag{61}$$

The spatial Fourier transform of (61) can be replaced by a fast Fourier transform in the analysis.

Table 1: Settings for phase velocity variation tests.
The background amplitudes and the relative polarization are varied. The large wavelength of the background manifests itself as an ever-persistent background.

Grid	Length	$100\mu m$
	Lattice Points	1000
Background	$\vec{A}_b$	$(0,60,0)\mu E_{cr}$ to $(0,1.5,0)E_{cr}$
	λ	$1Pm$
Probe	$\vec{A}_p$	$(0,1,0)$ and $(0,0,1)\mu E_{cr}$
	λ	$2\mu m$

To analyze the phase velocity variation numerically the background field strength is varied. In a second step the relative polarization of the waves is changed from parallel to orthogonal. The configurations are given in table 1. The total simulation time is chosen to be $200\mu m$, conveniently divided into 100 steps of $2\mu m$ – the chosen wavelength of the probe wave.
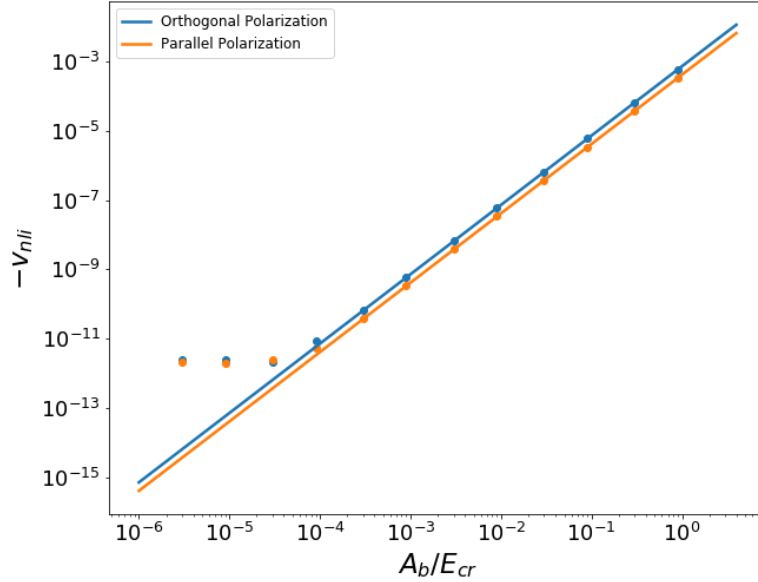
Figure 9: Nonlinear contribution to the phase velocity slow-down in a background with varying field strength. The results converge to a value $\approx 2 \times 10^{-12}$ for small background field strengths. This is the phase velocity reduction caused by the lattice itself due to numerical errors. This numerical effect is getting larger than the physical effect for $A_b < 10^{-4}E_{cr}$. The values for background field strengths larger than $5 \times 10^{-4}E_{cr}$ have a mean absolute percentage error of 1.8% for parallel relative polarization and 1.2% for orthogonal relative polarization. The first error is presumably larger since the probe wave is not a perfect "probe" and contributes with its own polarization.

It can be seen that the nonlinear interactions give note to themselves in a reduction of the phase velocity of the simulated waves in figure 9. For sufficiently large background field strengths the numerical values are in perfect agreement with the analytical predictions.

7. Polarization Flipping – Vacuum Birefringence

Polarization or helicity flipping of a probe pulse propagating through a strong pump pulse is a result of vacuum birefringence. The origin of the effect is again the breaking of the isotropy of space by the polarization of the strong background. The refractive indices from above

$$n_- = 1 + \frac{8\alpha}{45\pi}\frac{E^2}{E_{cr}^2} \quad \text{and} \quad n_+ = 1 + \frac{14\alpha}{45\pi}\frac{E^2}{E_{cr}^2} \tag{62}$$

generate a difference in optical path length for the probe pulse polarization components parallel and orthogonal to the pump polarization which results in *bi*refringence. On a microscopic level, a portion

of the pulse's quanta flip their polarization. Macroscopically, the overall polarization experiences a tiny turn.

A typical probe-pump scenario devised for the observation of helicity flips is shown in figure 10. A probe pulse in the x-ray regime propagates through a strong low-frequency pump field in which spatial isotropy is broken. A corresponding initial simulation configuration showing one polarization direction is depicted in figure 11.
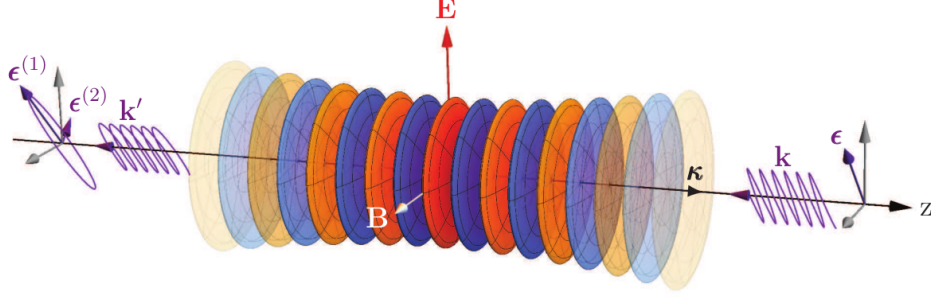

Figure 10: Sketch of the pump-probe type scenario intended to verify vacuum birefringence. A linearly polarized optical high-intensity laser pulse – wavevector κ, electric (magnetic) field $\mathbf{E}$ ($\mathbf{B}$) – propagates along the positive z-axis. Its strong electromagnetic field couples to the charged particle-antiparticle fluctuations in the quantum vacuum, and thereby effectively modifies its properties to be probed by a counter-propagating x-ray beam (wavevector k, polarization ϵ). Vacuum birefringence manifests itself in an ellipticity of the outgoing x-ray photons (wavevector k', polarization components along $\epsilon^{(1)}$ and $\epsilon^{(2)}$). Figure and caption taken from [25].
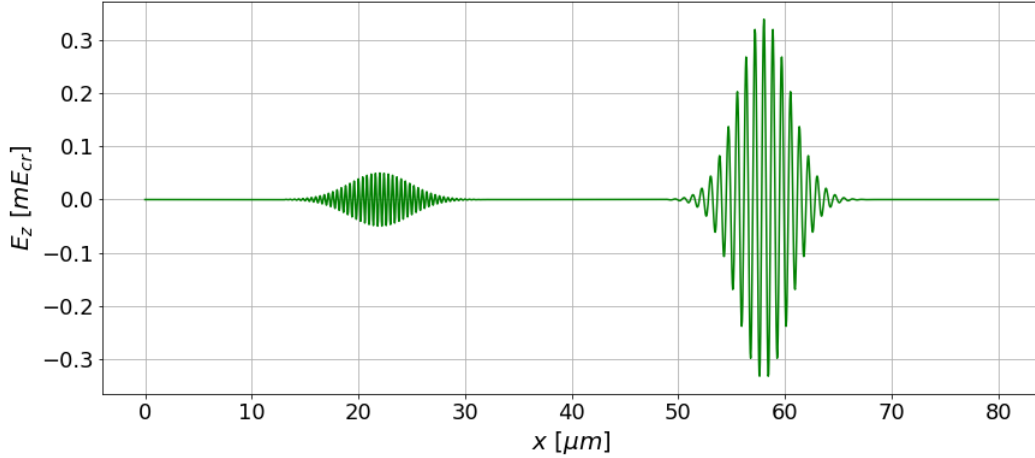

Figure 11: Sketch of the initial pulse configuration for the simulation of polarization flipping. On the left is the weak probe pulse which propagates to the right and on the right is the strong pump pulse propagating leftwards. Note that in the actual simulations the pump field strengths and probe frequencies are much larger than in this figure.

In order to backtest the numerical solver, firstly (subsection 7.1), parametric checks of the flipping probability as derived in [26] are performed. The settings given in table 2 are chosen to this end with Gaussian pulses pulses given by (64) below. With that result being verified, secondly (subsection 7.2), the scaling properties are made use of to attain the analytical result of a real-life calculation for a polarization flipping scenario calculated in [25]. The parameters for that setup are listed in table 3.

For both cases the normalized vectors parallel and orthogonal to the initial probe polarization are given as

$$\vec{\varepsilon}_\parallel = (0, 1/\sqrt{2}, 1/\sqrt{2}) \quad \text{and} \quad \vec{\varepsilon}_\perp = (0, -1/\sqrt{2}, 1/\sqrt{2}). \tag{63}$$

For the simulations 1D Gaussian pulses are used in the form

$$\vec{E} = \vec{A}\, e^{-(\vec{x}-\vec{x}_0)^2/\tau^2} \cos(\vec{k}\cdot\vec{x}). \tag{64}$$

The vector $\vec{A}$ comprises amplitude and polarization, $\vec{x}_0$ is the center of the pulse, τ its width, and $\vec{k}$ the wavevector. For convenience, the normalized vector $\hat{k}$ giving the propagation direction is stated in the

parameter tables. As pulses are simulated instead of single photon quanta the number of flipped photons is obtained via the pulse energies

$$\frac{N_\perp}{N} = \frac{\hbar\omega N_\perp}{\hbar\omega N} = \frac{\mathrm{E}_\perp}{\mathrm{E}_{tot}} \ , \tag{65}$$

where the energies in the respective polarization directions are proportional to the electric field strength projections squared

$$\mathrm{E}_\perp \sim \sum_{x_i \in \mathcal{C}} \left(\vec{E}(x_i) \cdot \vec{\varepsilon}_\perp \right)^2 , \quad \mathrm{E}_\parallel \sim \sum_{x_i \in \mathcal{C}} \left(\vec{E}(x_i) \cdot \vec{\varepsilon}_\parallel \right)^2 , \quad \mathrm{E}_{tot} = \mathrm{E}_\perp + \mathrm{E}_\parallel \ . \tag{66}$$

All other factors in (65) cancel.

7.1. Vacuum birefringence – parametrical dependencies

For coaxially counterpropagating unfocused pump and probe pulses the polarization flip probability, taking into account again only up to 4-photon interactions, in the low-energy approximation for a plane wave pump field is given by [26]

$$P_{\mathrm{flip}} = \frac{\alpha^2}{255\lambda_{\mathrm{probe}}^2} \sin^2(2\sigma) \left(\int dx \frac{E_{\mathrm{pump}}(x)^2}{E_{cr}^2} \right)^2 \ , \tag{67}$$

where σ is the angle between the probe and pump polarizations. The probe field strength is assumed to be negligible compared to the pump. The probability directly translates to the flip ratio

$$N_\perp = P_{\mathrm{flip}} \cdot N \ . \tag{68}$$

Formula (67) yields all the parametric dependencies for the probability of polarization flips and indirectly excludes other parameters. Note the strong dependence on the pump field strength and also on the probe wavelength. However, it is independent of the shape of the pulses. Deviations from the above formula for focused background pulses will be discussed in the next subsection. In 1D simulations the background can be modeled as a Gaussian. To investigate the scaling properties of the numerical solver the settings in table 2 are used. A time-resolved flipping process for those parameters is shown in figure 12. The results of the scaling tests are visualized in figure 13. There is perfect agreement between the 1D simulation results and formula (67). With these scaling properties being verified in the algorithm, the way is paved to reproduce the analytical result in case (a) of [25].

Table 2: Parameters for probe and pulse beam chosen to check the parametric dependencies in (67). The peak to peak distance at $t = 0$ is $36\,\mu$m. The probe wavelength, the pump field strength, and their relative polarization are varied to obtain the parametric dependencies in figure 13´.

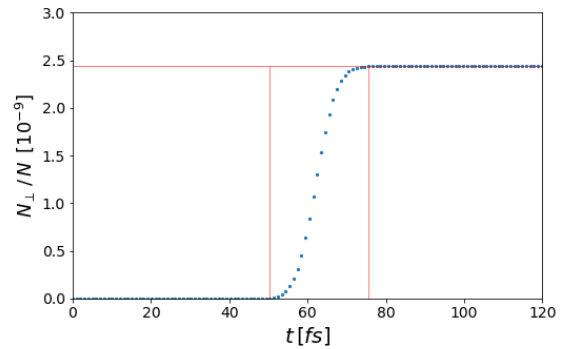| Grid	Length	$80\mu m$
	Lattice Points	1000
Pump	$\vec{A}$	$(0,0,34)\mathrm{m}E_{cr}$
	$\hat{k}$	(-1,0,0)
	λ	$800nm$
	$\vec{x}_0$	$58\mu m$
	τ	$3.5\mu m$
Probe	$\vec{A}$	$(0,50,50)\mu E_{cr}$
	$\hat{k}$	(1,0,0)
	λ	$25nm$
	$\vec{x}_0$	$22\mu m$
	τ	$4.0\mu m$

Figure 12: Time evolution of the polarization flipping ratio for the parameters presented in table 2. The distance between the vertical lines is the total interaction time $t_I=25$fs. The settings used here provide an interaction time of 25fs. The horizontal line corresponds to the asymptotic relative flip energy ratio.
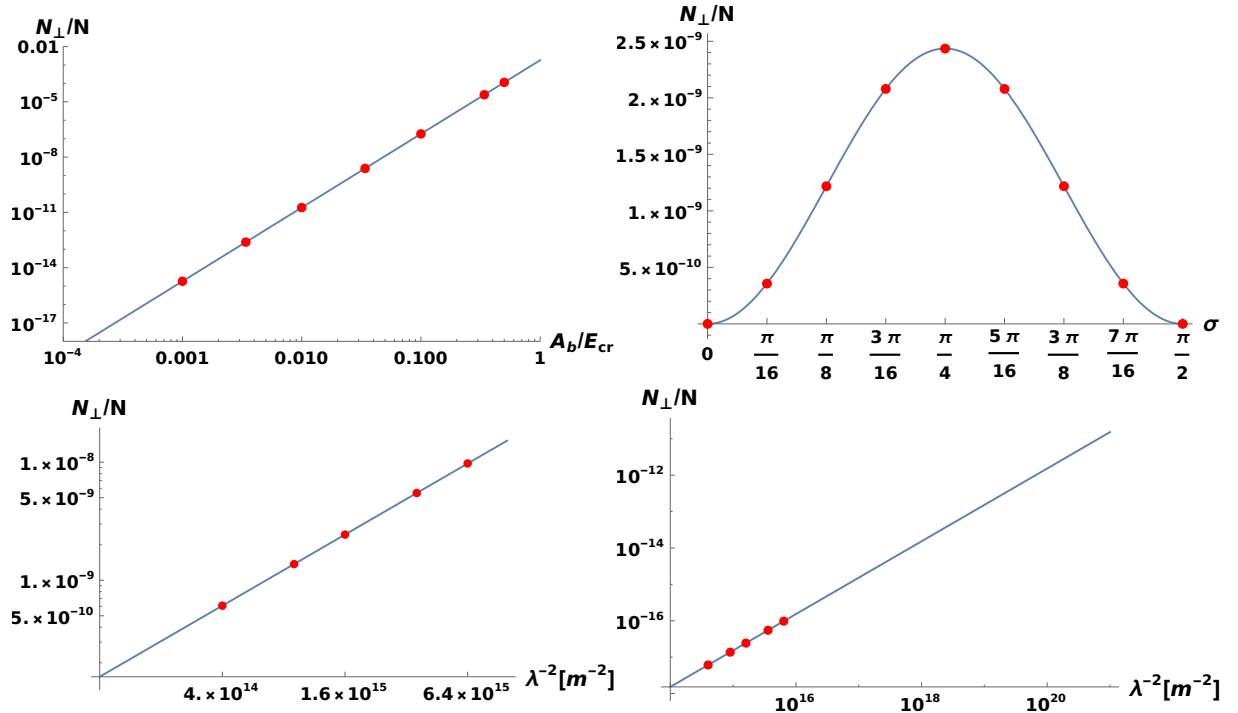
Figure 13: Scaling of the polarization flipping probability with variations of the parameters given in 2. The solid lines are obtained with (67). The red dots are simulation results. Top left: Varying the background field strength. Top right: Varying the relative polarization angle of probe and pump. Bottom left: Varying the probe wavelength. Bottom right: Combining the scaling of the pump field strength and probe wavelength – A_b is scaled down by a factor 100 compared to 2. Simultaneously an extrapolation to frequencies in the x-ray regime is performed. This last way of combining scaling properties is useful in order to extrapolate to relevant probe frequency scales while keeping the numerical accuracy high and the computational load low.

It has to be noted here, as it has also been found in [37], that there is a signal at $\sigma = \pi/2$ in the top right diagram of figure 13 with value 2.87×10^{-14}. This is above the numerical noise and due to harmonic generation. The polarization of a harmonic resulting from a higher order photon interaction is determined by energy conservation to be along the polarization of the pulse contributing with an uneven amount of photons. Hence, even though there should be no signal from polarization flipping, there are signals from harmonic generation. Harmonic generation is however not considered in formula (67). This example shows that the simulation algorithm yields all effects in one go in contrast to most analytical calculations. Combined effects like this are up to future research where the algorithmic solver will hopefully prove invaluable. Neglecting that signal, the mean absolute percentage errors in all the scaling plots above are below 0.1%.

7.2. Vacuum birefringence – extrapolation to an analytical value in the x-ray regime

The settings for the simulation of the scenario described in case (a) in [25] are given in table 3. For this real-life 3D scenario the techniques have to be adapted. First, the pump field strength is too low to extract the flipping process from the numerical noise. To combat this, it is being made use of the field strength scaling properties. Second, the chosen probe frequency is very high. An extremely fine grid would be necessary to model that pulse. To evade computations that expensive, the wavelength scaling properties can be made use of. It is thus a combination of two scaling methods in the way shown in the bottom right of figure 13 and described in the caption.

Furthermore, the 1D simulations do not take into account lateral dispersion (diffusion) effects of the focused background field as they are present in 3D. That deficiency is remedied by reducing the pump peak field strength to the average over the interaction time $t_I \simeq 23.5 fs$, see Fig. 14. The pump peak amplitude is thereby reduced from $0.34 \mathrm{m} E_{cr}$ to $0.29 \mathrm{m} E_{cr}$. This is a source of errors, especially when used for an extrapolation over several orders of magnitude. The results in figure 15 show that the extrapolation in principle works. The extrapolated value is 1.44×10^{-12} while the result in [25] is 1.39×10^{-12}.

Table 3: Parameters for probe and pulse beam adapted to [25].

The pump field strength is obtained as the square root of the ratio of intensity to critical intensity. Pump and probe are coaxially counterpropagating. The pulse durations are $30fs$. Furthermore, pump and probe polarizations are at an angle of $\pi/4$ and the initial peak to peak distance is $36\,\mu m$.

Grid	Length	$80\mu m$
	Lattice Points	1000
Pump	$\vec{A}$	$(0,0,0.34)\mathrm{m}E_{cr}$
	$\hat{k}$	$(-1,0,0)$
	λ	$800nm$
	$\vec{x}_0$	$58\mu m$
	τ	$4.5\mu m$
Probe	$\vec{A}$	$(0,50,50)\mu E_{cr}$
	$\hat{k}$	$(1,0,0)$
	λ	$96pm$
	$\vec{x}_0$	$22\mu m$
	τ	$3.4\mu m$
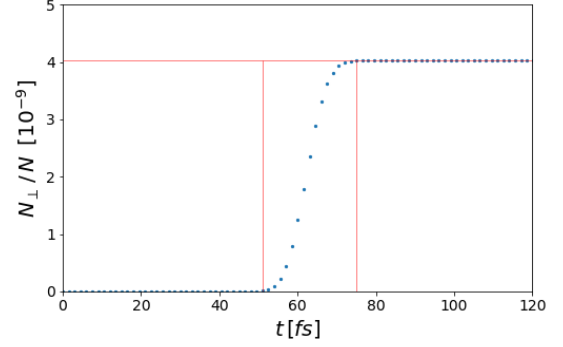
Figure 14: Time evolution of the polarization flip for an adaption of the parameters presented in table 3. The changes are: The pump field strength is magnified by a factor 100 to $34\mathrm{m}E_{cr}$ to reduce numerical noise. The probe wavelength is enlarged to the computationally acceptable value of 25nm. The distance between the vertical red lines is the total interaction time t_I=23.5fs. The horizontal red line denotes the asymptotic relative flip energy.
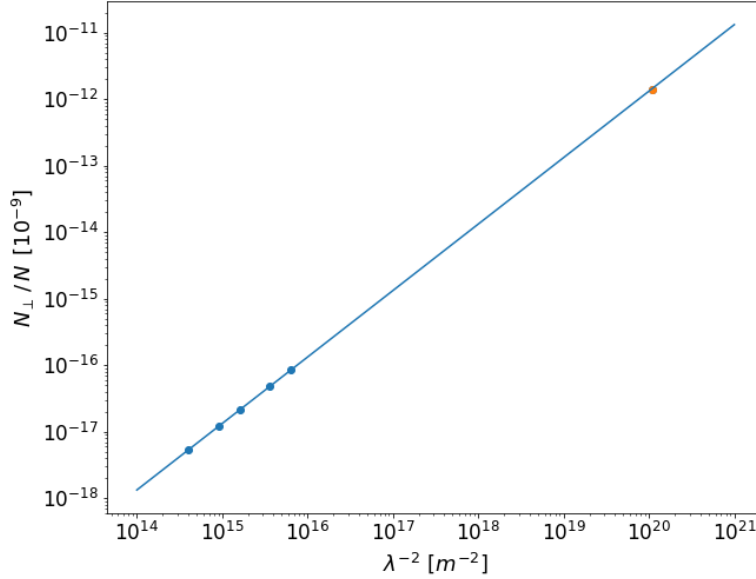

Figure 15: Extrapolation of polarization flipping ratios to high frequencies in 3D by emulating diffusion in 1D simulations. The blue line is an extrapolation of simulation results with various probe wavelengths (blue dots). The orange dot represents the value obtained in [25].

8. High Harmonic Generation

To backtest the algorithmic program the prominent scenario for the detection of nonlinear vacuum signatures depicted in figure 16 is considered again. For the present analysis two head-on colliding pulses are assumed, a weak probe pulse and a strong zero-frequency background pulse. The initial settings are listed in table 4.

Approximate analytical results for this scenario have been derived in [15, 17]. The effective vertices for 4- and 6-photon scattering in figure 17 (a) can produce higher-frequency outgoing photons by photon merging. As an example, in figure 17 (b) two probe photons and a zero-frequency background photon merge into an outgoing photon with frequency $2\omega_p$.

Table 4: Initial settings to observe harmonic generation in 1D simulations, see figure 16.

Grid	Length	$300\mu m$
	Lattice Points	4000
Pump	$\vec{A}$	$(0,20,0)\mathrm{m}E_{cr}$
	$\hat{k}$	(-1,0,0)
	λ	$1m$
	x_0	$200\mu m$
	τ	$12.8\mu m$
Probe	$\vec{A}$	$(0,5,0)\mathrm{m}E_{cr}$
	$\hat{k}$	(1,0,0)
	λ	$2\mu m$
	x_0	$100\mu m$
	τ	$10\mu m$
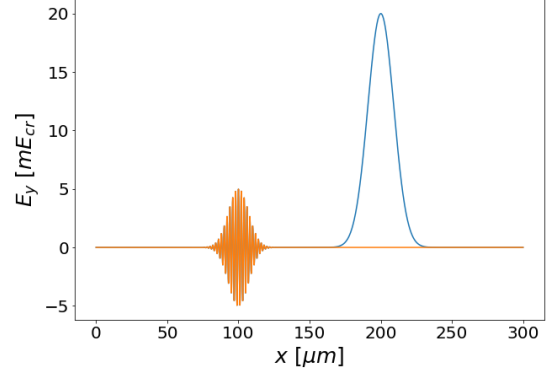
Figure 16: Visualization of the initial pulse configuration to detect higher harmonics with a zero-frequency background pulse, see table 4.

(a) Effective vertices for 4- and 6-photon scattering

(b) High-harmonic generation with a zero-frequency background
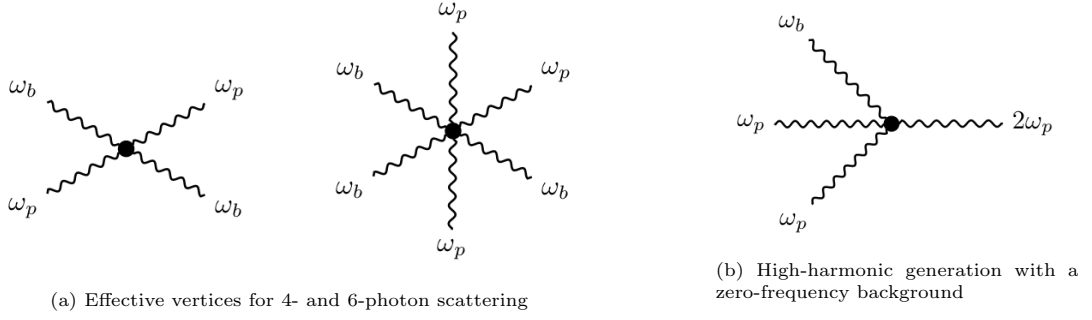
Figure 17: Feynman diagrams for harmonic generation. In (b) there is an implicit time axis from left to right.

The possible contributions of two wave scattering resulting from the the weak-field expansion are depicted in figure 18.

(a) $\omega_r \in \omega_b, 2\omega_p \pm w_b, \omega_p, \omega_p \pm 2\omega_b$

(b) $w_r \in \omega_b, 3\omega_b, \omega_p + 3\omega_b, 2\omega_p \mp 2\omega_b, \omega_p, \omega_p \mp 2\omega_b, 3\omega_p \mp 2\omega_b$
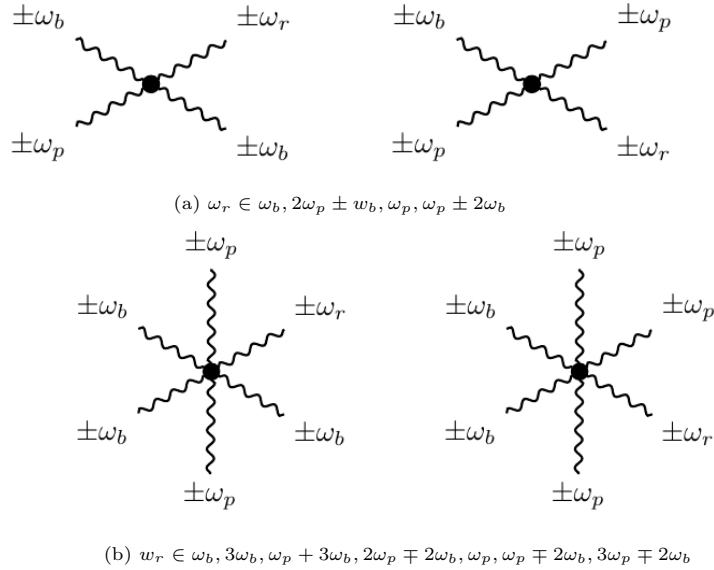
Figure 18: Allowed vertices and resulting frequencies ω_r for harmonic generation with 4-photon (a) and 6-photon (b) processes [15]. Further restrictions are posed upon the asymptotic states by energy conservation.

In the present case of $\omega_b = 0$ it is found for 4-photon and 6-photon processes.

4-photon processes

- The scattering of a background and a probe photon contributes with one photon to the zeroth harmonic ($\omega = 0$) and with one to the fundamental harmonic ($\omega = \omega_p$).

- Two background photons and one probe photon merge and produce a photon of the fundamental harmonic ($\omega = \omega_p$).

- Two probe photons and one background photon merge and produce a photon of the second harmonic ($\omega = 2\omega_p$).

6-photon processes

- The sheer scattering of background and probe photons contributes to the zeroth harmonic and the fundamental harmonic.

- Two background and two probe photons merge and produce one photon contributing to the second harmonic and one contributing to the zeroth harmonic.

- Two background and two probe photons merge and produce two photons contributing to the fundamental harmonic.

- Two background photons and three probe photons merge and produce a photon contributing to the third harmonic ($\omega = 3\omega_p$).

- The merging of three background and two probe photons produces a photon contributing to the second harmonic.

A visualization of the contributions is provided with figure 19. It can be seen that the asymptotic contribution to the second harmonic is only due to 6-photon processes. That is because *wave-mixing* – resulting pulses that are combined of photons of both pulses – is asymptotically not allowed. This is due to energy conservation for coaxial pulses, as for a photon resulting of wave mixing the following holds

$$k_{\text{res}}^{\mu} = n_p \, \omega_p \left(1, \hat{k}\right) + n_b \, \omega_b \left(1, -\hat{k}\right) \quad \text{and} \quad (k_{\text{res}}^{\mu})^2 = 0 \;\Rightarrow\; n_p \, n_b \overset{!}{=} 0 \; , \tag{69}$$

where n_p and n_b are the numbers of the contributing photons and $\hat{k}$ is the normalized propagation direction vector of the probe pulse. These states are thus only visible in the overlap configuration. The 6-photon process, on the other hand, can produce second harmonics without wave mixing, see the second point for six-photon processes above.

8.1. High harmonic generation – analytical results

Analytical methods in [15, 17] contain a derivation of iterative solutions to the nonlinear equations of motion for zero-frequency backgrounds. With the probe (p) and background (b) pulses as time-dependent 1D Gaussians with the parameters of table 4 the Gaussians are obtained to be, compared to (64),

$$\vec{E}_p(x;t) = \vec{\epsilon}_p \, A_p \, e^{-(k_p^{\mu} x_{\mu p})^2 / (\omega_p \tau_p)^2} \cos(k_p^{\mu} x_{\mu p}) \quad \text{and} \quad \vec{E}_b(x;t) = \vec{\epsilon}_b \, A_b \, e^{-(k_b^{\mu} x_{\mu b})^2 / (\omega_b \tau_b)^2} \; , \tag{70}$$

with $k_j^{\mu} x_{j\mu} = \omega_j t - \vec{k}_j \vec{x}_j$. The shifted coordinates of probe and background field read

$$\vec{x}_p = (x - 100\mu m, 0, 0) \quad \text{and} \quad \vec{x}_b = (x - 200\mu m, 0, 0) \; . \tag{71}$$

Writing a combined electric field as

$$\vec{E} = \vec{E}_p + \vec{E}_b \; , \tag{72}$$

the inhomogeneous wave equation in 1D can be written as

$$(\partial_t^2 - \partial_x^2) \, \vec{E} = T[\vec{E}] \; . \tag{73}$$

The source term T comprises the nonlinear Heisenberg-Euler interactions. Decomposing the electric field into

$$\vec{E} = \vec{E}^{(0)} + \vec{E}^{(1)} + \ldots \; , \tag{74}$$

where $\vec{E}^{(0)}$ solves the free vacuum wave equation $(\partial_t^2 - \partial_x^2) \, \vec{E}^{(0)} = 0$, an iterative procedure is obtained [15] in which

$$(\partial_t^2 - \partial_x^2) \, \vec{E}^{(1)} = T[\vec{E}^{(0)}] \; . \tag{75}$$

With the polarization for both fields given by

$$\vec{\epsilon} = (0, 1, 0) \tag{76}$$

and defining the shorthands

$$\kappa_p = \frac{k_p^\mu x_{\mu p}}{\omega_p \tau_p} \quad \text{and} \quad \kappa_b = \frac{k_b^\mu x_{\mu b}}{\omega_b \tau_b} \ , \tag{77}$$

it is then obtained for the solution to the nonlinear wave equation (75) at the first iterative order for

- the dc component (zeroth harmonic):
  The overlap field

$$\vec{E}_{0,o}^{(1)} = -\frac{8\alpha}{180\pi} A_p^2 \, \vec{E}_b(x;t) \, e^{-2\kappa_p^2} \, \vec{\epsilon} \tag{78}$$

  and the asymptotic field

$$\vec{E}_{0,a}^{(1)} = \frac{8\alpha}{180\pi} A_p^2 \sqrt{\frac{\pi}{2}} \frac{\tau_p \kappa_b}{\tau_b} (1 + \text{erf}(\sqrt{2}\kappa_b)) A_b \, e^{-\kappa_b^2} \, \vec{\epsilon} \ . \tag{79}$$

- the fundamental harmonic (first harmonic):
  The overlap field

$$\vec{E}_{1,o}^{(1)} = -\frac{8\alpha}{90\pi} A_p e^{-\kappa_p^2} \, \vec{E}_b(x;t)^2 \, \cos(k_p^\mu x_{p\mu}) \, \vec{\epsilon} \tag{80}$$

  and the asymptotic field

$$\vec{E}_{1,a}^{(1)} = \frac{8\alpha}{90\pi} A_p e^{-\kappa_p^2} A_b^2 \sqrt{\frac{\pi}{2}} \omega_p \tau_b \frac{1 + \text{erf}(\sqrt{2}\kappa_b)}{2} \, \sin(k_p^\mu x_{p\mu}) \, \vec{\epsilon} \ . \tag{81}$$

- the second harmonic:
  The overlap field

$$\vec{E}_{2,o}^{(1)} = -A_p^2 e^{-2\kappa_p^2} \left[\frac{8\alpha}{180\pi} \vec{E}_b(x;t)^2 + \frac{96\alpha}{630\pi} \vec{E}_b(x;t)^3 \right] \cos(2k_p^\mu x_{p\mu}) \, \vec{\epsilon} \tag{82}$$

  and the asymptotic field

$$\vec{E}_{2,a}^{(1)} = \frac{96\alpha}{315\pi} A_p^2 e^{-2\kappa_p^2} A_b^3 \sqrt{\frac{\pi}{3}} \omega_p \tau_b \frac{1 + \text{erf}(\sqrt{3}\kappa_b)}{2} \, \sin(2k_p^\mu x_{p\mu}) \, \vec{\epsilon} \ . \tag{83}$$

- the third harmonic:
  The overlap field

$$\vec{E}_{3,o}^{(1)} = -\frac{96\alpha}{1260\pi} A_p^3 e^{-3\kappa_p^2} \, \vec{E}_b(x;t)^2 \, \cos(3k_p^\mu x_{p\mu}) \, \vec{\epsilon} \tag{84}$$

  and the asymptotic field

$$\vec{E}_{3,a}^{(1)} = 0 \ . \tag{85}$$

Using the values from table 4 the solid blue transparent lines in figure 20 are obtained. Those are employed to scrutinize the efforts.
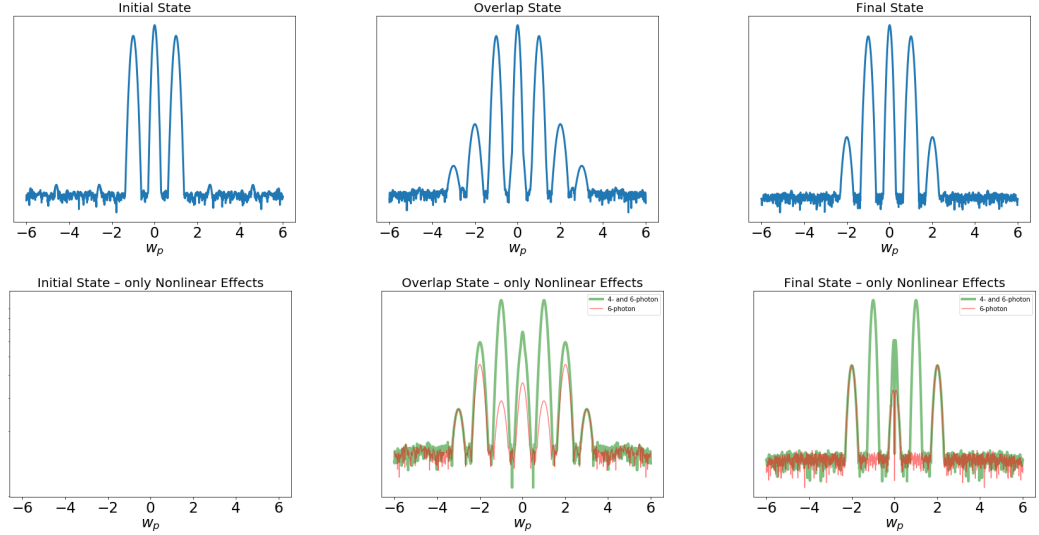
Figure 19: A log scale makes the higher harmonics visible in frequency space. Top: a full simulation of the linear vacuum supplemented by 4- and 6-photon nonlinear interactions. Bottom: after subtraction of the linear vacuum. The initial state contains only the main signals that disappear without the linear terms. The overlap state is the time step where the pulses are directly overlapping, at the final state they have separated again – the asymptotic field is left. It can be deduced that the third harmonic and the asymptotic part of the second harmonic are only due to 6-photon processes.

8.2. High harmonic generation – simulation results

The interest lies predominantly in the nonlinear contributions to the generation of harmonics. There-fore, each setting is simulated three times with varying combinations of interactions included. Once in-cluding only the nonlinear effects of four- and six-photon contributions. Once including only six-photon processes. Once excluding all nonlinear interactions, i.e., only the linear vacuum. By subtracting the dynamics in the linear vacuum from the nonlinear dynamics the higher order processes of the weak-field expansion are extracted. The simulations of six-photon processes allow to isolate their sole contribution. It is a nice feature of the simulation code that the contributions of 4- and 6-photon diagrams can be turned on and off to make them separately visible. See figure 19.

In order to extract the amplitudes of the various arising harmonics and their time evolution, their respective frequencies have to be filtered in Fourier space by setting all others to zero and then trans-forming back to position space [37]. The amplitude is obtained directly as the maximum norm and its time evolution can be observed. The results for the zeroth harmonic (dc component), first harmonic (fundamental harmonic), second, and third harmonic are shown in figure 20.
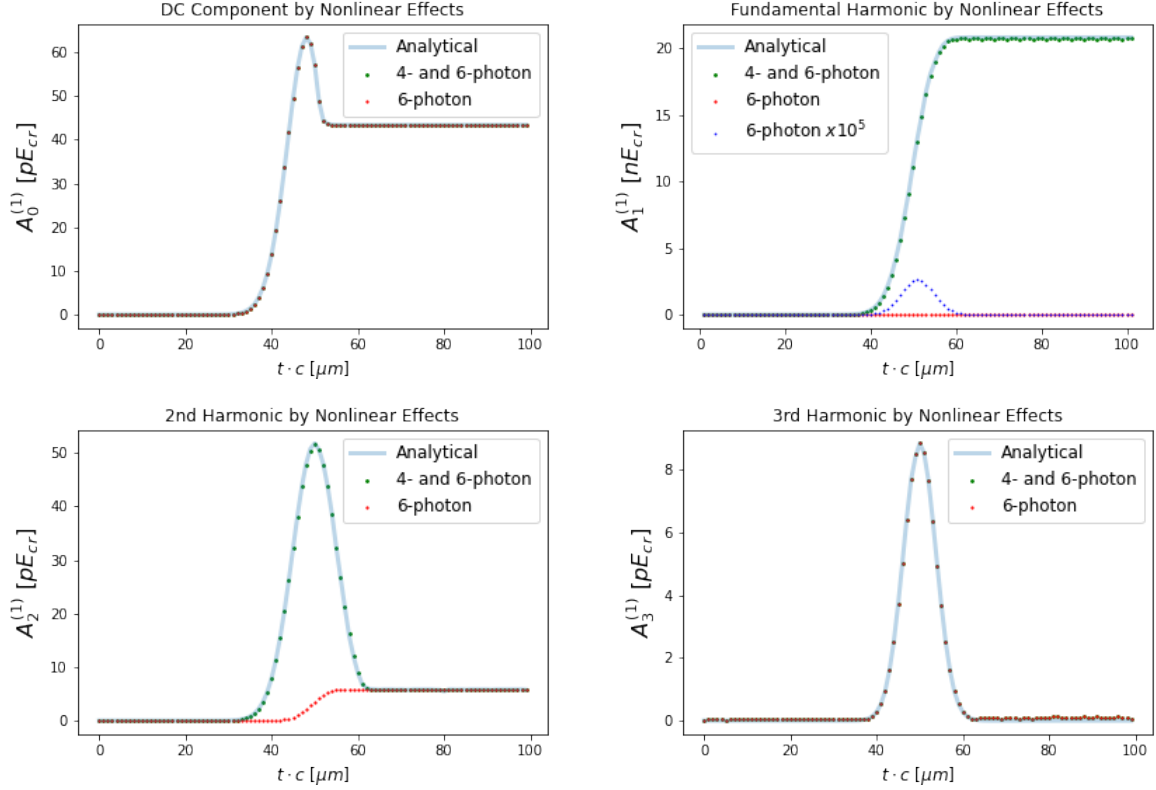
Figure 20: Time evolution of the harmonics amplitudes caused by 4- and 6-photon processes combined and only by 6-photon processes after subtraction of the linear vacuum propagation. Dots in brown (color overlap of green and red) indicate an overlap of 6-photon processes with the combined values for 4- and 6-photon processes. Analytical approximations obtained in (78)-(85) are underlying as the blue transparent curve. There are systematic errors due to back and forth Fourier transforming as well as the slicing of frequency ranges.

As can be seen in figure 20 there is good agreement between the analytical approximation and the simulation results. There are systematic errors due to the back and forth Fourier transformation and slicing of frequency ranges. The mean absolute percentage errors of the simulation results are calculated to be less than 1% in the regions where the amplitudes are non-vanishing.

Asymptotic states are constrained by energy-momentum conservation, while the overlap state has a richer spectrum. This spectrum becomes especially versatile when the pulses collide at a nonzero angle, which is a task for future work of higher-dimensional simulations. First results are demonstrated in section 9.

In the next section and subsequent works, the zero-frequency background restriction will be relaxed and the pulses will collide at a non-zero angle. Signals which are degenerate in the case of a one zero-frequency pulse will split up. Simulations in higher dimensions provide a means to analyze varying collision configurations. Situations that pose no further difficulty to the code are considerably hard to cope with analytically. Employing simulations of this algorithm it is possible to track harmonic frequencies in time and space for scenarios of arbitrary pulse parameters – with the only restrictions posed by the applicability of the Heisenberg-Euler weak-field expansion and computational feasibility.

9. 2D Simulations

For simulations in 2D a special adaption of 3D Gaussian pulses is used to model the diffusion behavior. The pulse propagates along $z(t) = t - z$. The beam waist of the pulse at position z is given by

$$w(z) = w_0 \sqrt{1 + \left(\frac{z - z_0}{z_R}\right)^2} \tag{86}$$

with w_0 as the waist of the beam at position z_0, where the amplitude is $1/e$ of the initial value. The field intensity scales with $w_0/w(z)$ and with the surface area $\sim z^2$ in 3D. Lateral dispersion has to be taken into account in the 2D Gaussians, where the surface scales as $\sim z$. Hence, the factor $w_0/w(z)$ appearing

as prefactor in the Gaussian pulses gets a square root in the lower dimensional case. The pulse can thus be written as

$$\vec{E}(r, z(t)) = A\,\vec{\epsilon}\,\sqrt{\frac{w_0}{w(z)}}\,e^{-(r/w(z))^2}\,e^{-((z-z_\tau)/\tau_z)^2}\,\cos\left(\frac{k\,r^2}{2R(z)} + \zeta(z) - kz\right)\ . \tag{87}$$

It has further been defined

- the pulse amplitude A and polarization $\vec{\epsilon}$,
- the radial coordinate $r = \sqrt{x^2 + y^2 + z^2}$,
- the wavenumber $k = 2\pi/\lambda$,
- the pulse width in z-direction τ_z and the envelope center z_τ,
- the Rayleigh length $z_R = \pi w_0^2/\lambda$ as the longitudinal distance from z_0 at which the waist has increased by a factor $\sqrt{2}$. It is contained in
- the Gouy phase $\zeta(z) = \arctan(z/z_R)$, and
- the beam curvature $R(z) = z(1 + (z_R/z)^2)$.

The settings used for 2D simulations are listed in table 5.

Table 5: Settings for 2D simulations with two conceptually equal Gaussian pulses. The wavelength is obtained via $\lambda = \pi w_0^2/z_R$.

Grid	Square Size	$80\mu m \times 80\mu m$
	Lattice Points	1024×1024
Pulse 1	$\vec{\epsilon}$	(0,0,1)
	A	$50\mathrm{m}E_{cr}$
	$\hat{k}$	$(1,0,0)\mu m$
	λ	$1\mu m$
	w_0	$2.3\mu m$
	z_R	$16.619\mu m$
	z_τ	$20\mu m$
	τ_z	$4.5\mu m$
Pulse 2	same parameters as pulse 1, but different center position, varying propagation direction and polarization	see figure 21-28

Comparing a head-on collision in 1D (figure 19) and 2D (figure 21) a similar frequency spectrum is found at the different time states. The reasoning is the same as in section 8. The main difference stems from the fact that the two conceptionally equal pulses have the same *non-zero* frequency. There is still a degeneracy of signals present due to the equal frequencies.

As an extra feature not available in the 1D simulation a broadening of the signals in frequency space is observed – and an according sharpening of the pulse in position space which is hardly visible – in the asymptotic state. This is mostly due to 4-photon interactions as it is caused by birefringence effects that are stronger in the center of the pulses. Thus, post-collision pulses are sharper in position space and broader in the frequency domain.

Going beyond coaxial pulses by varying the collision angle and thereby lifting the degeneracy of frequencies of the harmonics, very rich spectra in 2D simulations can be observed, see figures 23-26 for perpendicularly propagating and colliding pulses as well as for an angle of 135°. Nearly all signals vanish again in the asymptotic state. In the overlap states various merging processes become directly visible, e.g. in the overlap state of perpedicularly colliding pulses the merging processes of 3ω and 2ω harmonics. The asymptotic states propagate only along the initial propagation axis.

Giving the pulses' different polarization directions, the harmonics can be tagged. The frequency space of the simulations visualized in figures 27 and 28 show again collision angles of 90°and 135°, but the pulse

propagating from the right is now polarized along E_y. Hence, the shown components can be identified with one of the two pulses. The E_z component is to be associated to the pulse coming from the left which keeps the E_z polarization, and the B_z component to that coming from the right. Hereby the harmonic signals are tagged as they obtain the polarization of the pulse that contributes an odd amount of photons.
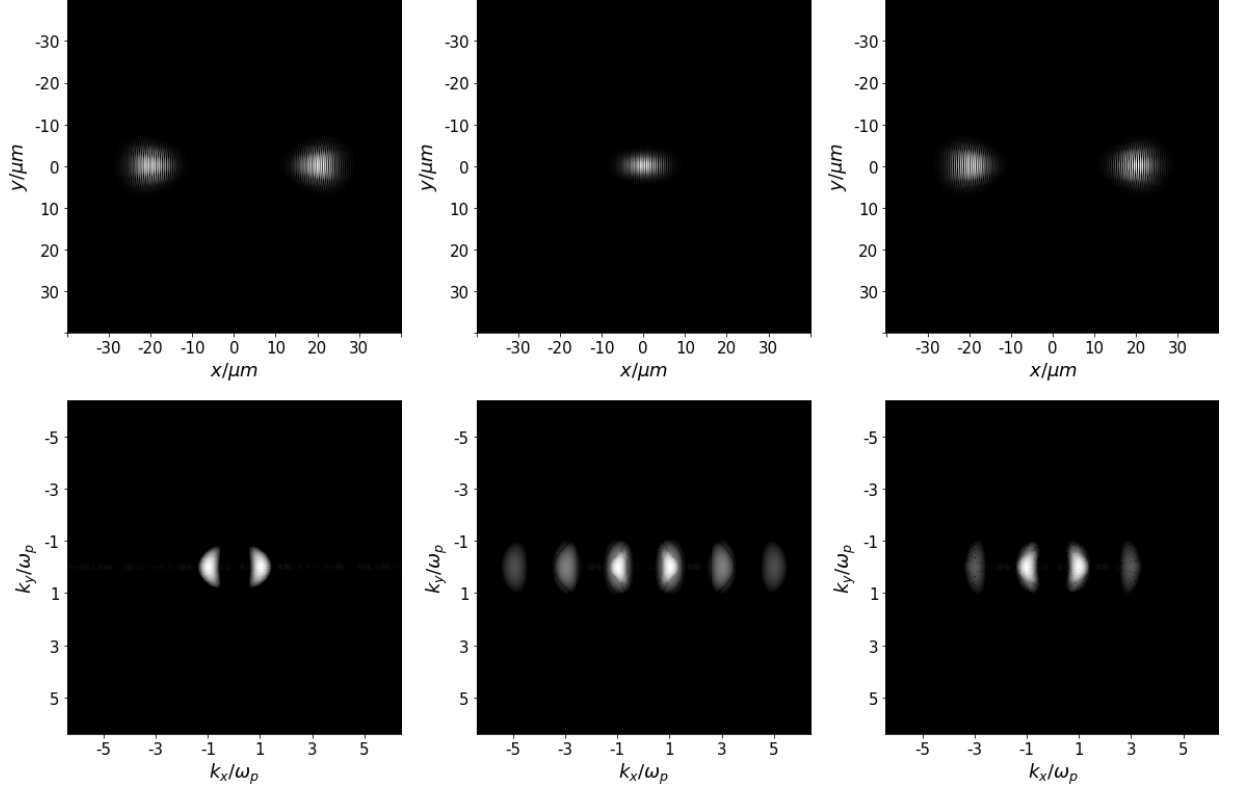

Figure 21: Coaxially colliding pulses with the same polarization. The left plots show the initial state, those in the middle the overlap state, and the right ones the final state. Top: position space. Bottom: frequency space.
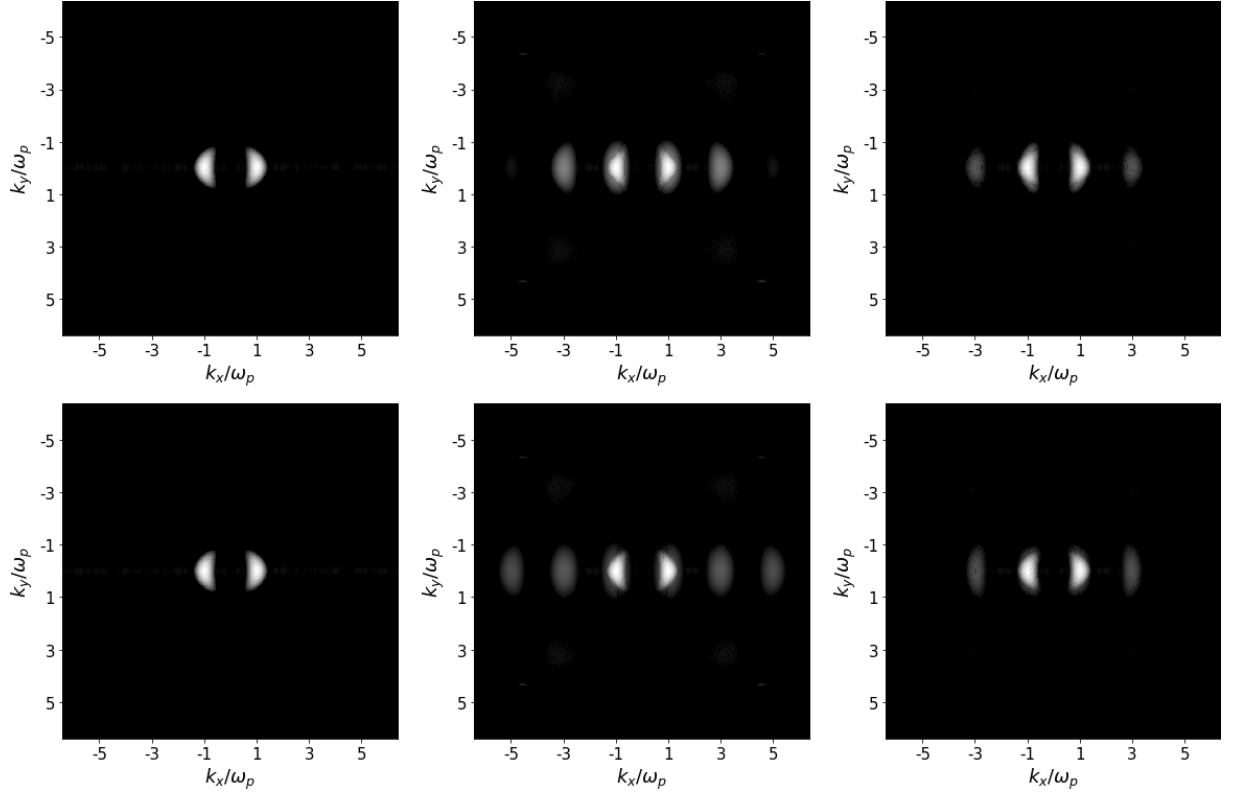
Figure 22: Frequency space of coaxially colliding pulses with the same polarization. The left plots show the initial state, those in the middle the overlap state, and the right ones the final state. Top: only 4-photon diagrams included. Bottom: only 6-photon diagrams included.
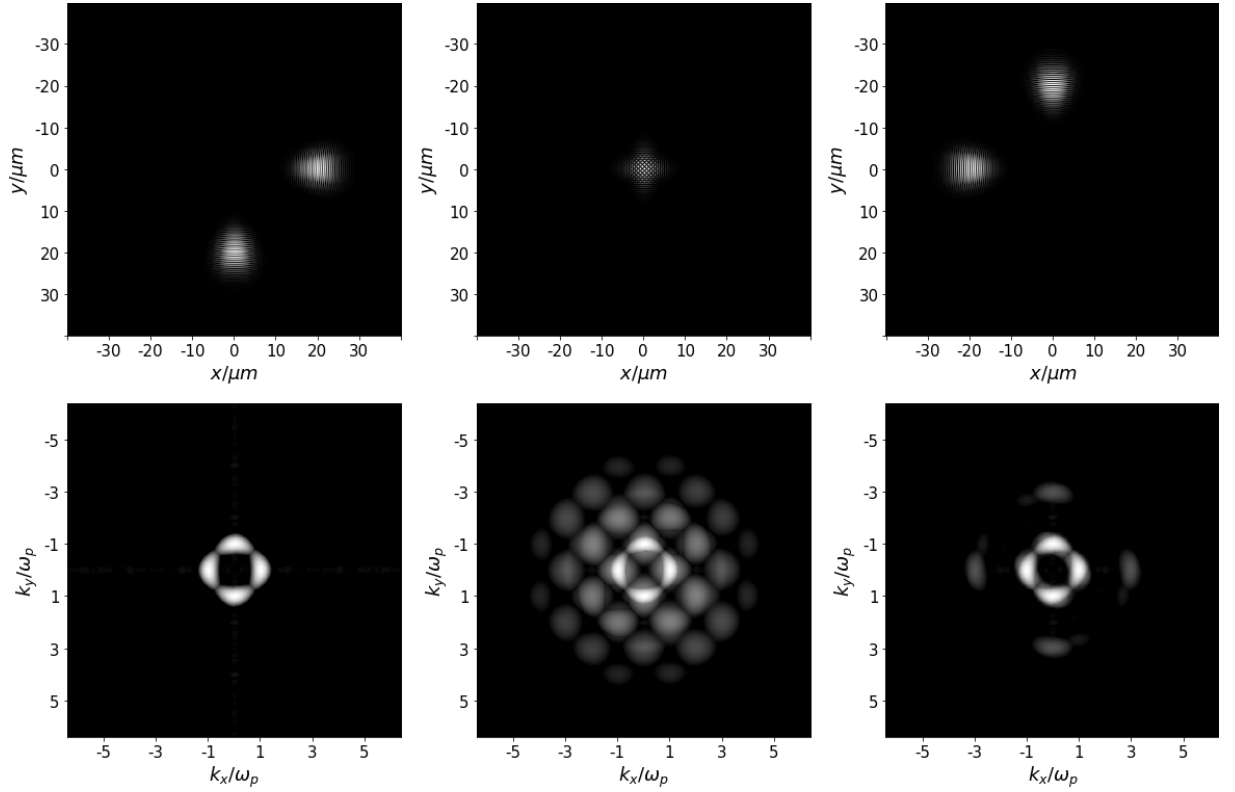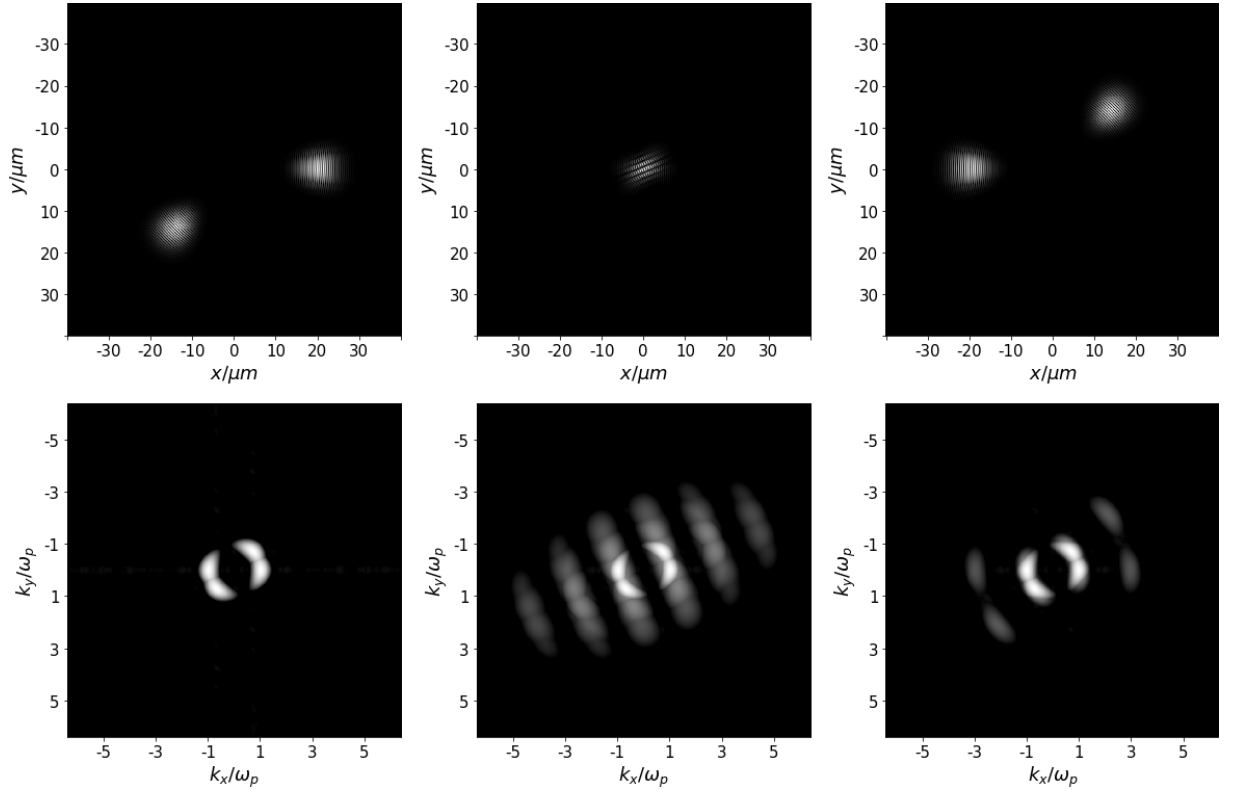

Figure 23: Perpendicularly colliding pulses with equal polarization. The left plots show the initial state, those in the middle the overlap state, and the right ones the final state. Top: position space. Bottom: frequency space.
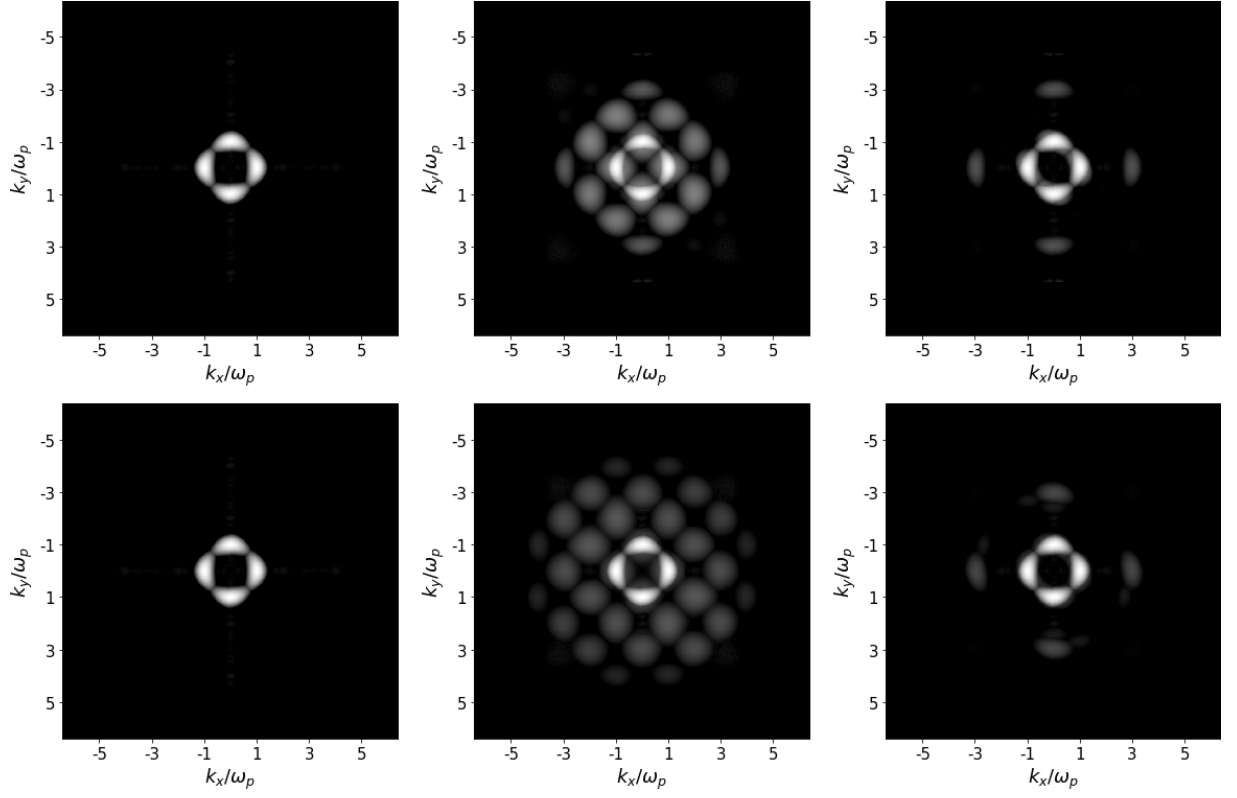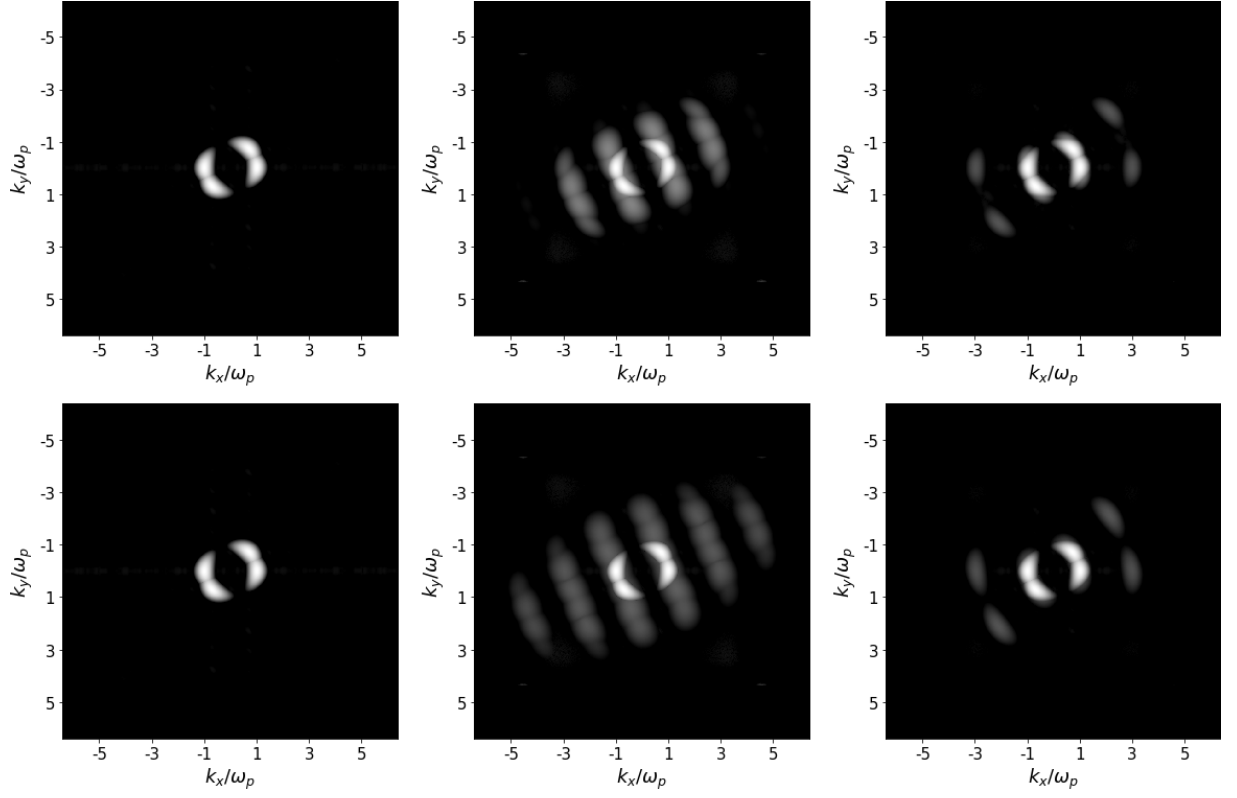
Figure 24: Frequency space of orthogonally colliding pulses with same polarization. The left plots show the initial state, those in the middle the overlap state, and the right ones the final state. Top: only 4-photon diagrams included. Bottom: only 6-photon diagrams included.

Figure 25: Pulses with the same polarization colliding at an angle of 135°. The left plots show the initial state, those in the middle the overlap state, and the right ones the final state. Top: position space. Bottom: frequency space.

Figure 26: Frequency space of pulses with the same polarization colliding at an angle of 135°. The left plots show the initial state, those in the middle the overlap state, and the right ones the final state. Top: only 4-photon diagrams included. Bottom: only 6-photon diagrams included.
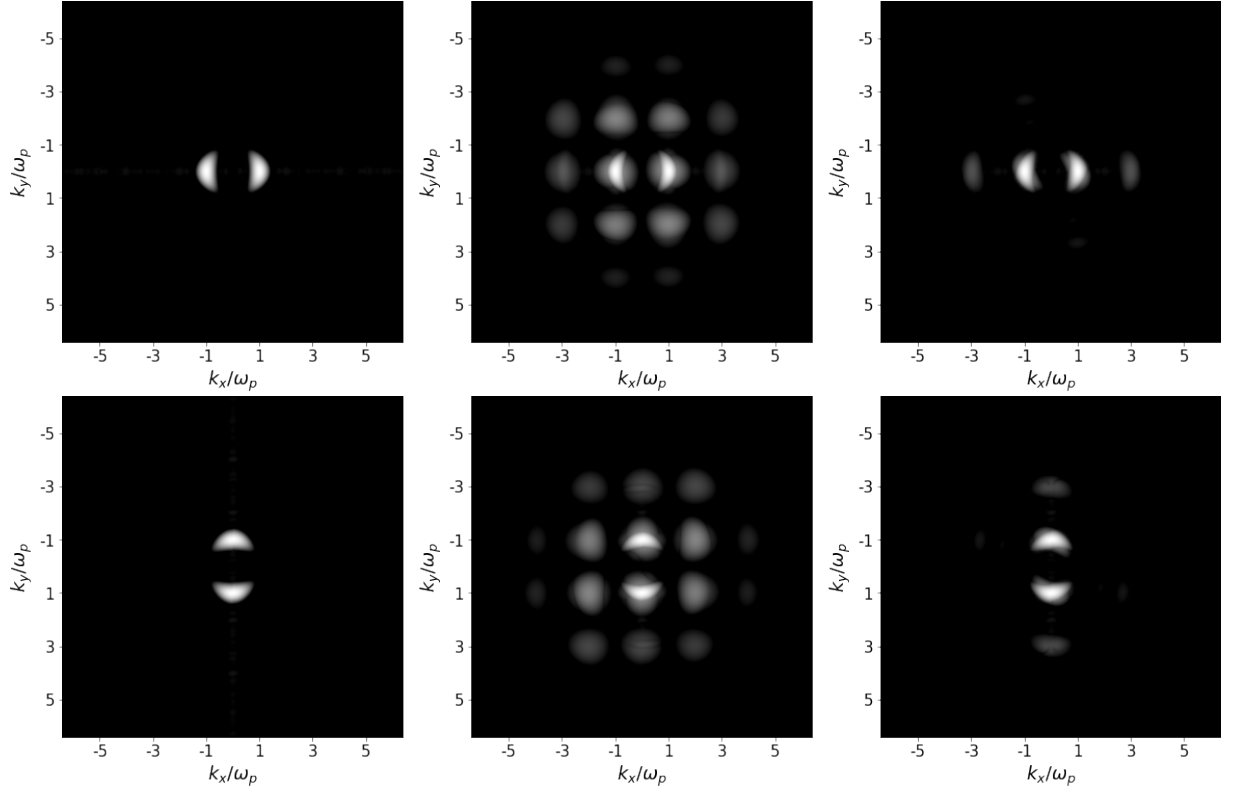

Figure 27: Frequency space of perpendicularly colliding pulses with orthogonal relative polarization. The left plots show the initial state, those in the middle the overlap state, and the right ones the final state. Top: the E_z component is shown. Bottom: the B_z component is shown.
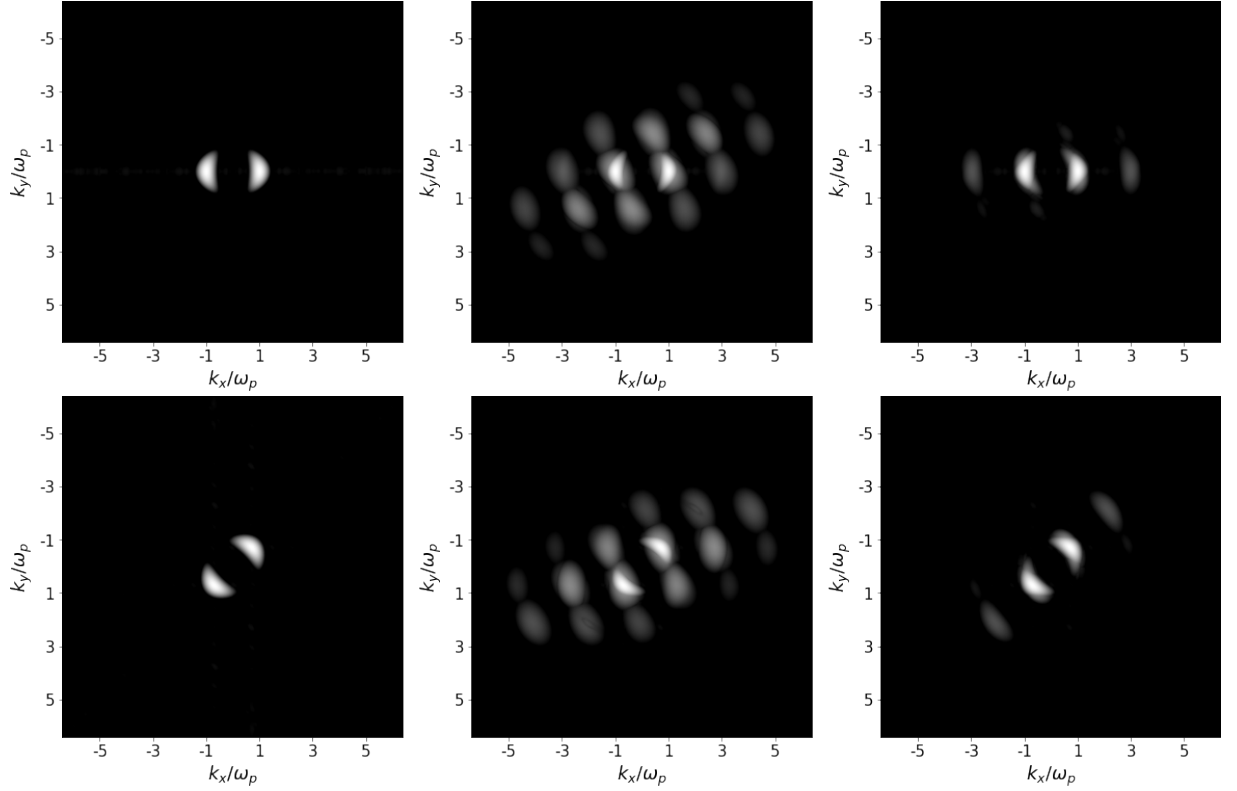
Figure 28: Frequency space of pulses colliding at an angle of 135° with orthogonal relative polarization. The left plots show the initial state, those in the middle the overlap state, and the right ones the final state. Top: the E_z component is shown. Bottom: the B_z component is shown.

10. Conclusion and Outlook

A numerical scheme solving the Heisenberg-Euler equations in 3+1 dimensions in the weak-field expansion has been presented. The basic assumptions restrict to field strengths below the critical values and wavelengths larger than the Compton length of the electron.

The current C++ implementation allows simulations for up to 6-photon processes and, remarkably, distinct simulations for the linear Maxwell vacuum, only 4-photon processes, or only 6-photon processes. Every simulation includes the complete picture of the Heisenberg-Euler nonlinear physics. This means that the observation of single effects does not in principle require tailored settings, but everything is contained in any output simultaneously. Analytical calculations normally concentrate on single effects alone, leaving others aside. Special effects of interest are extracted by a proper dedicated post-processing.

Since all simulations can be divided into an arbitrary number of time steps, the simulations allow to time-resolve any process, which is beyond the scope of many analytical approaches concentrating on asymptotic values alone.

The numerical complexity scales considerably fast with the number of lattice points, the resolution, and the dimension. It has to be stated again here that a sufficiently high grid resolution is demanded by the dispersion relation for well-behaved waves. The resolution has to be tuned in wise prospect to the signals which are attempted to be observed. Therefore, the computations become costly quite fast.

The fact that not individual photon quanta but whole pulses are simulated is not hampering the analysis. On the contrary, it is striking to see such good agreement to analytical results.

The scope of this code is far-reaching. The main purpose of the present paper is to introduce the simulation algorithm and to prove its validity. As a proven solver of the Heisenberg-Euler dynamics its usefulness in today's strong-field QED research is indisputable. Not only the high-energy, low-intensity regime employed in particle accelerators, but also the low-energy, high-intensity regime might be a path towards new physics [48]. As the quantum fluctuations in the vacuum theoretically consist of all particles there are, it may also serve as a portal to new physics [31].

As a use case it is planned to conduct a characterization of strong pulses by propagating probe pulses through them and analyzing the asymptotic states of the latter. This should go under the name of "tomographic methods". The approach is to ultimately subside detector material when the intensities become too high. There has been theoretical work on such scattering configurations that may serve as a benchmark [32].

In ongoing studies the behavior of simulated waves at a grid resolution barrier is investigated. This research is intended to pave the way for a dynamical grid which adapts its resolution on the fly and on demand in order to reduce the computational load while at the same time maximizing the accuracy in important spatial regions.

Furthermore, it is the authors' aim to provide colleagues in the research group who study optical signatures of vacuum effects in high intensity fields with numerical results. To this end it will be attempted to reproduce the settings and findings of [31, 33–35]. The goal is to provide an indispensable tool for experimentalists to second their setups with simulation data.

In a follow-up work a first phenomenological analysis in 3D has to be performed. Besides the scaling test no results are shown of 3D simulations in this paper due to the heavy numerical load required to produce sensible data. A current task is thus the improvement of large scalability as mentioned in section 5. Ultimately, these simulations are intended run on major high performance computing facilities like the SuperMUC which is accessible to the authors. It is a huge step forward to finally go beyond lower dimensional approximations on the numerical side.

Aknowledgments

References

[1] W. Heisenberg, H. Euler, Folgerungen aus der diracschen theorie des positrons, Zeitschrift für Physik 98 (11) (1935) 714–732. `doi:10.1007/BF01343663`.
URL `http://dx.doi.org/10.1007/BF01343663`

[2] J. Schwinger, On gauge invariance and vacuum polarization, Phys. Rev. 82 (1951) 664–679. `doi:10.1103/PhysRev.82.664`.
URL `http://link.aps.org/doi/10.1103/PhysRev.82.664`

[3] J. Toll, The dispersion relation for light and its application to problems involving electron pairs, Ph.D. thesis, Princeton University, (unpublished) (1952).

[4] R. Baier, P. Breitenlohner, The vacuum refraction index in the presence of external fields, Il Nuovo Cimento B Series 10 47 (1) (1967) 117–120. `doi:10.1007/BF02712312`.
URL `http://dx.doi.org/10.1007/BF02712312`

[5] T. Heinzl, B. Liesfeld, K.-U. Amthor, H. Schwoerer, R. Sauerbrey, A. Wipf, On the observation of vacuum birefringence, Optics Communications 267 (2) (2006) 318 – 321. `doi:http://dx.doi.org/10.1016/j.optcom.2006.06.053`.
URL `http://www.sciencedirect.com/science/article/pii/S0030401806006481`

[6] B. J. King, Vacuum polarisation effects in intense laser fields, Ph.D. thesis, Ruprecht-Karls-Universität Heidelberg (2010).
URL `https://archiv.ub.uni-heidelberg.de/volltextserver/10846/`

[7] D. Tommasini, H. Michinel, Light by light diffraction in vacuum, Phys. Rev. A 82 (2010) 011803. `doi:10.1103/PhysRevA.82.011803`.
URL `http://link.aps.org/doi/10.1103/PhysRevA.82.011803`

[8] Y. Monden, R. Kodama, Enhancement of laser interaction with vacuum for a large angular aperture, Phys. Rev. Lett. 107 (2011) 073602. `doi:10.1103/PhysRevLett.107.073602`.
URL `http://link.aps.org/doi/10.1103/PhysRevLett.107.073602`

[9] A. Di Piazza, K. Z. Hatsagortsyan, C. H. Keitel, Light diffraction by a strong standing electromagnetic wave, Phys. Rev. Lett. 97 (2006) 083603. `doi:10.1103/PhysRevLett.97.083603`.
URL `https://link.aps.org/doi/10.1103/PhysRevLett.97.083603`

[10] B. King, A. Di Piazza, C. H. Keitel, A matterless double slit, Nature Photonics 4 (2) (2010) 92–94.
URL https://www.nature.com/articles/nphoton.2009.261#citeas

[11] S. L. Adler, Photon splitting and photon dispersion in a strong magnetic field, Annals of Physics 67 (2) (1971) 599 – 647. doi:http://dx.doi.org/10.1016/0003-4916(71)90154-0.
URL http://www.sciencedirect.com/science/article/pii/0003491671901540

[12] B. King, C. H. Keitel, Photon–photon scattering in collisions of intense laser pulses, New Journal of Physics 14 (10) (2012) 103002.
URL http://stacks.iop.org/1367-2630/14/i=10/a=103002

[13] H. Gies, F. Karbstein, N. Seegert, Quantum reflection as a new signature of quantum vacuum nonlinearity, New Journal of Physics 15 (8) (2013) 083002.
URL http://stacks.iop.org/1367-2630/15/i=8/a=083002

[14] P. Böhl, B. King, H. Ruhl, Vacuum high-harmonic generation in the shock regime, Phys. Rev. A 92 (2015) 032115. doi:10.1103/PhysRevA.92.032115.
URL http://link.aps.org/doi/10.1103/PhysRevA.92.032115

[15] P. A. Böhl, Vacuum harmonic generation in slowly varying electromagnetic backgrounds, Ph.D. thesis, lmu (2016).
URL https://edoc.ub.uni-muenchen.de/19887

[16] A. Fedotov, N. Narozhny, Generation of harmonics by a focused laser beam in the vacuum, Physics Letters A 362 (1) (2007) 1–5.
URL https://doi.org/10.1016/j.physleta.2006.09.085

[17] B. King, P. Böhl, H. Ruhl, Interaction of photons traversing a slowly varying electromagnetic background, Phys. Rev. D 90 (2014) 065018. doi:10.1103/PhysRevD.90.065018.
URL http://link.aps.org/doi/10.1103/PhysRevD.90.065018

[18] Z. Bialynicka-Birula, I. Bialynicki-Birula, Nonlinear effects in quantum electrodynamics. photon propagation and photon splitting in an external field, Phys. Rev. D 2 (1970) 2341–2345. doi:10.1103/PhysRevD.2.2341.
URL https://link.aps.org/doi/10.1103/PhysRevD.2.2341

[19] A. Di Piazza, A. I. Milstein, C. H. Keitel, Photon splitting in a laser field, Phys. Rev. A 76 (2007) 032103. doi:10.1103/PhysRevA.76.032103.
URL https://link.aps.org/doi/10.1103/PhysRevA.76.032103

[20] C. N. Danson, C. Haefner, J. Bromage, T. Butcher, J.-C. F. Chanteloup, E. A. Chowdhury, A. Galvanauskas, L. A. Gizzi, J. Hein, D. I. Hillier, et al., Petawatt and exawatt class lasers worldwide, High Power Laser Science and Engineering 7 (2019) e54. doi:10.1017/hpl.2019.36.
URL https://doi.org/10.1017/hpl.2019.36

[21] M. Scholz, FEL Performance Achieved at European XFEL, in: Proc. 9th International Particle Accelerator Conference (IPAC'18), Vancouver, BC, Canada, April 29-May 4, 2018, no. 9 in International Particle Accelerator Conference, JACoW Publishing, Geneva, Switzerland, 2018, pp. 29–33, https://doi.org/10.18429/JACoW-IPAC2018-MOZGBD2. doi:doi:10.18429/JACoW-IPAC2018-MOZGBD2.
URL http://jacow.org/ipac2018/papers/mozgbd2.pdf

[22] E. Lundstrom, G. Brodin, J. Lundin, M. Marklund, R. Bingham, J. Collier, J. T. Mendonca, P. Norreys, Using high-power lasers for detection of elastic photon-photon scattering, Phys. Rev. Lett. 96 (2006) 083602. arXiv:hep-ph/0510076, doi:10.1103/PhysRevLett.96.083602.

[23] J. Lundin, M. Marklund, E. Lundstrom, G. Brodin, J. Collier, R. Bingham, J. T. Mendonca, P. Norreys, Detection of elastic photon-photon scattering through four-wave mixing using high power lasers, Phys. Rev. A 74 (2006) 043821. arXiv:hep-ph/0606136, doi:10.1103/PhysRevA.74.043821.

[24] D. Tommasini, A. Ferrando, H. Michinel, M. Seco, Precision tests of QED and non-standard models by searching photon-photon scattering in vacuum with high power lasers, JHEP 11 (2009) 043. arXiv:0909.4663, doi:10.1088/1126-6708/2009/11/043.

[25] F. Karbstein, H. Gies, M. Reuter, M. Zepf, Vacuum birefringence in strong inhomogeneous electromagnetic fields, Phys. Rev. D 92 (2015) 071301. doi:10.1103/PhysRevD.92.071301.
URL http://link.aps.org/doi/10.1103/PhysRevD.92.071301

[26] V. Dinu, T. Heinzl, A. Ilderton, M. Marklund, G. Torgrimsson, Vacuum refractive indices and helicity flip in strong-field qed, Phys. Rev. D 89 (2014) 125003. `doi:10.1103/PhysRevD.89.125003`.
URL `http://link.aps.org/doi/10.1103/PhysRevD.89.125003`

[27] V. Dinu, T. Heinzl, A. Ilderton, M. Marklund, G. Torgrimsson, Photon polarization in light-by-light scattering: Finite size effects, Phys. Rev. D 90 (2014) 045025. `doi:10.1103/PhysRevD.90.045025`.
URL `http://link.aps.org/doi/10.1103/PhysRevD.90.045025`

[28] H. Gies, F. Karbstein, C. Kohlfürst, N. Seegert, Photon-photon scattering at the high-intensity frontier, Phys. Rev. D 97 (7) (2018) 076002. `arXiv:1712.06450`, `doi:10.1103/PhysRevD.97.076002`.

[29] H. Gies, F. Karbstein, C. Kohlfürst, All-optical signatures of Strong-Field QED in the vacuum emission picture, Phys. Rev. D 97 (3) (2018) 036022. `arXiv:1712.03232`, `doi:10.1103/PhysRevD.97.036022`.

[30] B. King, H. Hu, B. Shen, Three-pulse photon-photon scattering, Phys. Rev. A 98 (2) (2018) 023817. `arXiv:1805.03688`, `doi:10.1103/PhysRevA.98.023817`.

[31] F. Karbstein, A. Blinne, H. Gies, M. Zepf, Boosting quantum vacuum signatures by coherent harmonic focusing, Phys. Rev. Lett. 123 (2019) 091802. `doi:10.1103/PhysRevLett.123.091802`.
URL `https://link.aps.org/doi/10.1103/PhysRevLett.123.091802`

[32] F. Karbstein, E. A. Mosman, X-ray photon scattering at a focused high-intensity laser pulse, Phys. Rev. D 100 (2019) 033002. `doi:10.1103/PhysRevD.100.033002`.
URL `https://link.aps.org/doi/10.1103/PhysRevD.100.033002`

[33] F. Karbstein, Probing vacuum polarization effects with high-intensity lasers, Particles 3 (1) (2020) 39–61. `doi:10.3390/particles3010005`.
URL `https://www.mdpi.com/2571-712X/3/1/5`

[34] F. Karbstein, E. A. Mosman, Enhancing quantum vacuum signatures with tailored laser beams, Phys. Rev. D 101 (2020) 113002. `doi:10.1103/PhysRevD.101.113002`.
URL `https://link.aps.org/doi/10.1103/PhysRevD.101.113002`

[35] L. Klar, Detectable optical signatures of qed vacuum nonlinearities using high-intensity laser fields, Particles 3 (1) (2020) 223–233. `doi:10.3390/particles3010018`.
URL `https://www.mdpi.com/2571-712X/3/1/18`

[36] A. P. Domenech, H. Ruhl, An implicit ode-based numerical solver for the simulation of the heisenberg-euler equations in 3+1 dimensions (2017). `arXiv:1607.00253`.

[37] A. Pons Domenech, Simulation of quantum vacuum in higher dimensions, Ph.D. thesis, lmu (2018).
URL `https://edoc.ub.uni-muenchen.de/21885/`

[38] G. V. Dunne, T. M. Hall, Borel summation of the derivative expansion and effective actions, Phys. Rev. D 60 (1999) 065002. `doi:10.1103/PhysRevD.60.065002`.
URL `http://link.aps.org/doi/10.1103/PhysRevD.60.065002`

[39] H. Gies, L. Roessler, Vacuum polarization tensor in inhomogeneous magnetic fields, Phys. Rev. D 84 (2011) 065035. `doi:10.1103/PhysRevD.84.065035`.
URL `http://link.aps.org/doi/10.1103/PhysRevD.84.065035`

[40] J. C. Maxwell, A dynamical theory of the electromagnetic field, Philosophical Transactions of the Royal Society of London 155 (1865) 459–512. `doi:10.1098/rstl.1865.0008`.
URL `http://rstl.royalsocietypublishing.org/content/155/459.short`

[41] W. H. Press, S. A. Teukolsky, W. T. Vetterling, B. P. Flannery, Numerical Recipes 3rd Edition: The Art of Scientific Computing, 3rd Edition, Cambridge University Press, 2007.

[42] A. C. Hindmarsh, P. N. Brown, K. E. Grant, S. L. Lee, R. Serban, D. E. Shumaker, C. S. Woodward, SUNDIALS: Suite of nonlinear and differential/algebraic equation solvers, ACM Transactions on Mathematical Software (TOMS) 31 (3) (2005) 363–396.

[43] P. Virtanen, R. Gommers, T. E. Oliphant, M. Haberland, T. Reddy, D. Cournapeau, E. Burovski, P. Peterson, W. Weckesser, J. Bright, S. J. van der Walt, M. Brett, J. Wilson, K. J. Millman, N. Mayorov, A. R. J. Nelson, E. Jones, R. Kern, E. Larson, C. J. Carey, İ. Polat, Y. Feng, E. W. Moore, J. VanderPlas, D. Laxalde, J. Perktold, R. Cimrman, I. Henriksen, E. A. Quintero, C. R.

Harris, A. M. Archibald, A. H. Ribeiro, F. Pedregosa, P. van Mulbregt, SciPy 1.0 Contributors, SciPy 1.0: Fundamental Algorithms for Scientific Computing in Python, Nature Methods 17 (2020) 261–272. `doi:10.1038/s41592-019-0686-2`.

[44] T. Kluyver, B. Ragan-Kelley, F. Pérez, B. Granger, M. Bussonnier, J. Frederic, K. Kelley, J. Hamrick, J. Grout, S. Corlay, P. Ivanov, D. Avila, S. Abdalla, C. Willing, Jupyter notebooks – a publishing format for reproducible computational workflows, in: F. Loizides, B. Schmidt (Eds.), Positioning and Power in Academic Publishing: Players, Agents and Agendas, IOS Press, 2016, pp. 87 – 90.

[45] W. R. Inc., Mathematica, Version 12.3, champaign, IL (2021).
URL `https://www.wolfram.com/mathematica`

[46] L. Clarke, I. Glendinning, R. Hempel, The mpi message passing interface standard, in: Programming environments for massively parallel distributed systems, Springer, 1994, pp. 213–218.

[47] W. Dittrich, H. Gies, Probing the Quantum Vacuum: Perturbative Effective Action Approach in Quantum Electrodynamics and its Application, Springer Tracts in Modern Physics, Springer Berlin Heidelberg, 2003.
URL `https://books.google.de/books?id=lctrCQAAQBAJ`

[48] H. Gies, Strong laser fields as a probe for fundamental physics, Eur. Phys. J. D 55 (2009) 311–317. `arXiv:0812.0668`, `doi:10.1140/epjd/e2009-00006-0`.